The Astrophysical Journal, 815:18 (17pp), 2015 December 10 doi:10.1088/0004-637X/815/1/18

YOUNG GALAXY CANDIDATES IN THE *HUBBLE* FRONTIER FIELDS. II. MACS J0416–2403

Leopoldo Infante[1], Wei Zheng[2], Nicolas Laporte[1], Paulina Troncoso Iribarren[1], Alberto Molino[3,4], Jose M. Diego[5], Franz E. Bauer[1,6,7], Adi Zitrin[8,16], John Moustakas[9], Xingxing Huang[10], Xinwen Shu[11], David Bina[12], Gabriel B. Brammer[13], Tom Broadhurst[14,15], Holland C. Ford[2], Stefano García[1], and Sam Kim[1]
[1] Instituto de Astrofísica and Centro de Astroingeniería, Facultad de Física, Pontificia Universidad Católica de Chile, Vicuña Mackenna 4860, 7820436 Macul, Santiago, Chile
[2] Department of Physics and Astronomy, Johns Hopkins University, Baltimore, MD 21218, USA
[3] Instituto de Astronomía, Geofísica e Ciências Atmosféricas, Universidade de São Paulo, Cidade Universitária, 05508-090, São Paulo, Brazil
[4] Instituto de Astrofísica de Andalucía—CSIC, Glorieta de la Astronomía, s/n. E-18008, Granada, Spain
[5] IFCA, Instituto de Física de Cantabria, UC-CSIC, s/n. E-39005 Santander, Spain
[6] Millennium Institute of Astrophysics, Vicuña Mackenna 4860, 7820436 Macul, Santiago, Chile
[7] Space Science Institute, Boulder, CO 80301, USA
[8] Cahill Center for Astronomy and Astrophysics, California Institute of Technology, MC 249-17, Pasadena, CA 91125, USA
[9] Department of Physics and Astronomy, Siena College, Loudonville, NY 12211, USA
[10] Department of Astronomy, University of Science and Technology of China, Hefei, Anhui 230026, China
[11] Department of Physics, Anhui Normal University, Wuhu, Anhui, 241000, China
[12] IRAP, CNRS—14 Avenue Edouard Belin—F-31400 Toulouse, France
[13] Space Telescope Science Institute, 3700 San Martin Drive, Baltimore, MD 21218, USA
[14] Department of Theoretical Physics, University of Basque Country UPV/EHU, Bilbao, Spain
[15] IKERBASQUE, Basque Foundation for Science, Bilbao, Spain
Received 2015 March 2; accepted 2015 October 23; published 2015 December 2

ABSTRACT

We searched for $z \gtrsim 7$ Lyman-break galaxies in the optical-to-mid-infrared *Hubble* Frontier Field and associated parallel field observations of the strong-lensing cluster MACS J0416−2403. We discovered 22 candidates, of which 6 lie at $z \gtrsim 9$ and 1 lies at $z \gtrsim 10$. Based on the *Hubble* and *Spitzer* photometry, all have secure photometric redshifts and a negligible probability of being at lower redshifts according to their peak-probability ratios, $\mathcal{R}$. This substantial increase in the number of known high-redshift galaxies allows a solid determination of the luminosity function (LF) at $z \gtrsim 8$. The number of high-z candidates in the parallel field is considerably higher than that in the Abell 2744 parallel field. Our candidates have median stellar masses of $\log(M_*) \sim 8.44^{+0.55}_{-0.31}\,M_\odot$, star formation rates (SFRs) of $\sim 1.8^{+0.5}_{-0.4}\,M_\odot\,\mathrm{yr}^{-1}$, and SFR-weighted ages of $\lesssim 300^{+70}_{-140}$ Myr. Finally, we are able to put strong constraints on the $z = 7$, 8, 9, and 10 LFs. One of the objects in the cluster field is a $z \simeq 10$ candidate, with a magnification of $\mu \sim 20 \pm 13$. This object is likely the faintest $z \sim 10$ object known to date, allowing a first look into the extreme faint end ($L \sim 0.04\,L^*$) of the $z \sim 10$ LF (It is named "Tayna" in the Aymara language).

Key words: cosmology: observations – galaxies: clusters: individual (MACS0416) – galaxies: high-redshift – gravitational lensing: strong

1. INTRODUCTION

The universe at $z \sim 10$ was approximately $330\,h^{-1}$ million years old. At this time, galaxy assembly was well underway and the intergalactic medium (IGM) was being reionized by UV radiation (presumably from the first stars and compact objects). These two processes mark an important era in the evolution of the universe. In that sense, it is important to understand how different young galaxies are from local ones and how their numbers evolve with redshift.

In the last few years the number of galaxies discovered at the highest redshifts has increased dramatically (Bouwens et al. 2011a, 2012; Ellis et al. 2013; Illingworth et al. 2013; Oesch et al. 2013; Bouwens et al. 2015; Bradley et al. 2014). For instance, in 2008 only a handful of $z \gtrsim 7$ galaxies were known and none had been discovered above $z \sim 8$; today these numbers have grown to ∼300 for $z \sim 7$, ∼100 for $z \sim 8$, and even ∼10 at $z \sim 10$. Of particular interest is the latest result by the *Planck* collaboration on the optical depth to reionization, τ. The cosmic microwave background (CMB) power spectrum is sensitive to τ both in the temperature power spectrum and in the polarization power spectrum. The CMB data is not sensitive to the particular model of reionization but is very sensitive to its average redshift. The latest results from *Planck* suggest a lower value for τ than previous estimates from *WMAP* data. The new value for the optical depth ($\tau = 0.066 \pm 0.016$) translates into a mean redshift of reionization of $z \approx 8$ (Planck Collaboration et al. 2015). When combined with recent measurements of the Ly-α forest that suggest that reionization of the intergalactic medium was nearly complete by $z \approx 6$ (Fan et al. 2006), a simple picture of the reionzation history can be put together in which reionization may have happened gradually between $z = 10$ and $z = 6$. The lack of galaxies beyond $z = 10$ in our deep fields supports this hypothesis, and we may already be discovering the first galaxies emerging from the dark ages. Under the simple hypothesis that reionization happened gradually between $z = 10$ and $z = 6$ and that this reionization took place in a patchy form, we should expect a statistically significant variability in the number density of detected galaxies at $z \approx 10$ when comparing different deep fields (for instance from the *Hubble* Frontier Fields (HFF, Lotz et al. 2014) program since some of them may reach further in redshift.

The increase in the number of known high-redshift galaxy candidates is mainly due to the advent of new instrumentation

[16] Hubble Fellow.

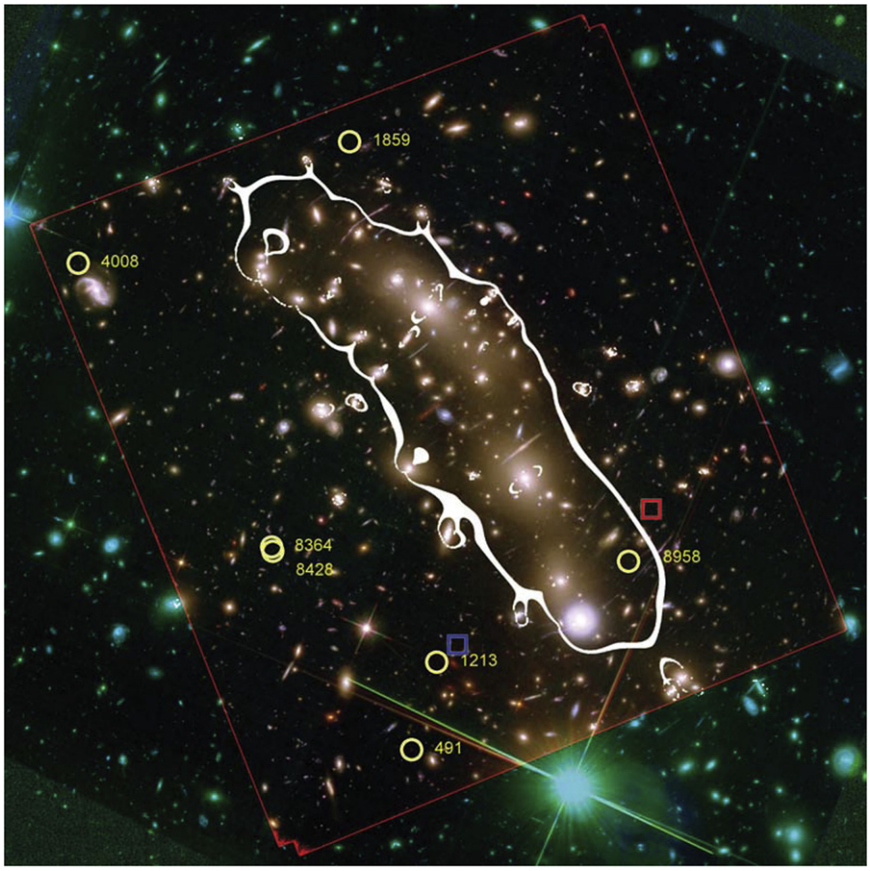

Figure 1. $3' \times 3'$ *HST* color image of the M0416 cluster field, comprising the ACS F606W (blue), ACS F814W (green), and WFC3 F160W (red) bands, with the $z = 10$ critical curve from the Diego et al. (2015) lens mass model overlaid. Our $z > 7$ candidates are labeled and marked with yellow circles. The red and blue squares are model predictions for 8958 potential counter images. The typical error in the position for this solution is approximately 3 arcsec, which is the size of the boxes.

on the *Hubble Space Telescope* (*HST*) Wide-Field Camera 3/Infrared Channel (WFC3/IR, Kimble et al. 2008), coupled with constraints from the *Spitzer Space Telescope* Infrared Array Camera (IRAC, Fazio et al. 2004). How far can we push these instruments to probe the first galaxies? At $z \gtrsim 10$, galaxies are extremely faint. Most have intrinsic luminosities fainter than $M_* \simeq -19.5$ and sizes of a few hundreds of parsecs (see Zheng et al. 2012b; Coe et al. 2013; Bouwens et al. 2014a, 2015; Bradley et al. 2014; Kawamata et al. 2015; Zitrin et al. 2014). To observe them, one option is to take advantage of gravitational lensing by massive galaxy clusters, which magnifies and shears background galaxy light as it passes through the cluster. To achieve detections, two crucial elements are needed: high enough amplification, which is provided by observing massive galaxy clusters, and accurate photometric redshifts, which are obtained by observing a large number of wavelength bands with accurate photometry. Of course, to retrieve the intrinsic source properties of the distant objects requires very good mass lens models of the cluster. This confluence of data has been secured by two recent *HST* cluster surveys, the Cluster Lensing And Supernova survey with *Hubble* (CLASH, Postman et al. 2012) and the HFF.

The HFF campaign (560 *HST* orbits of Director's Discretionary Time) in particular was designed to take advantage of *HST*'s unsurpassed spatial resolution and sensitivity. Four clusters of galaxies are being observed in Cycles 21 and 22 and two more are expected in Cycle 23.[17] Observations are carried out with the *HST* Advanced Camera for Surveys (ACS) in three optical bands (F435W, F606W, and F814W) and with *HST* WFC3 in four NIR bands (F105W, F125W, F140W, and F160W), to limiting magnitudes of ∼29–30 AB. These are (or will be) complemented by deep *Spitzer* and *Chandra* observations of these six clusters. The *HST* HFF observations have now been completed for clusters Abell 2744 and MACS J0416 −2403 (hereafter A2744 and M0416, respectively) and have resulted in dozens of publications. Among these Zheng et al. (2014) reported the discovery of 24 Lyman-break candidates between $7 \lesssim z \lesssim 10.5$ and a triple system with a photometric redshift of $z_{\rm ph} \simeq 7.4$ in A2744, Zitrin et al. (2014) reported the geometrical confirmation of a multiply-lensed $z \sim 10$ object in A2744, Laporte et al. (2015) communicated the discovery of four bright $z \sim 8$ galaxies in M0416, and McLeod et al. (2014) reported the discovery of $z \sim 8$–9 galaxies in M0416 (see also Atek et al. 2014; Ishigaki et al. 2015).

In this paper (the second in our discovery series), we report the discovery of 22 $z \gtrsim 7$ galaxy candidates in the HFF cluster M0416 and parallel fields. We analyze their physical properties via spectral energy distribution (SED) fitting and combine results from A2744 and M0416 to compute luminosity functions (LFs) at redshifts $z \simeq 7-8-9$ and 10. The $z \sim 8$ galaxy candidates in M0416 from Laporte et al. (2015) are also used in our analysis. In Section 2 we describe the observations

[17] See http://www.stsci.edu/hst/campaigns/frontier-fields/documents/HDFI_SWGReport2012.pdf

Table 1
Summary of Observations

Telescope	Band	Exposure Time (s)	Limiting Magnitude (5σ)
		M0416	
HST	F435W	54512	29.2
HST	F606W	35450	29.2
HST	F814W	131897	29.3
HST	F105W	72567	29.0
HST	F125W	39302	28.7
HST	F140W	29870	28.6
HST	F160W	74787	28.8
VLT/HAWK-I	K_s	97440	26.5
Spitzer	IRAC1	340712	25.3
Spitzer	IRAC2	340712	25.3
		Parallel Field	
HST	F435W	45747	29.0
HST	F606W	25035	28.9
HST	F814W	95406	29.2
HST	F105W	79912	29.1
HST	F125W	34248	28.5
HST	F140W	34248	28.6
HST	F160W	79912	28.8
VLT/HAWK-I	K_s	97440	26.5
Spitzer	IRAC1	340712	25.3
Spitzer	IRAC2	340712	25.3

Table 2
IRAC Photometry for Selected Candidates[a]

Name	IRAC1	IRAC2
	M0416	
8958	>25.31	>25.75
1859	>26.67	>27.11
8364[b]	26.59 ± 0.52	25.79 ± 0.23
491	>27.07	24.72 ± 0.20
1213	>26.67	>26.76
8428[b]	26.73 ± 0.60	25.93 ± 0.26
4008	>25.32	>25.54
	Parallel Field	
3687	>27.54	>27.76
4177	>26.41	>26.59
3076	>26.92	>27.69
1301	>27.22	>27.45
3814	>27.52	>27.10
1241	>27.22	>27.45
5296[c]	23.22 ± 0.73	22.66 ± 0.02
3790	>26.64	>26.70
4125	26.65 ± 0.30	26.58 ± 0.25
6999	>27.30	>27.40
7361	>27.32	>27.27
1331	>27.93	>27.78
1386	>26.72	>27.01
1513	26.96 ± 0.44	26.62 ± 0.26
146	>27.26	>27.85

Notes.
[a] The symbol ">" represents 1σ upper limits on no detection.
[b] 8364 and 8428 are within 2 pixels from each other in IRAC images. We estimated their IRAC flux based on the F160W band flux ratio.
[c] This object is contaminated by a nearby spiral galaxy. The photometry is largely uncertain.

and the data; Section 3 details how galaxies are selected; the lens models and photometric redshift estimations are presented in Section 4; and in Section 5 we present an SED fitting analysis, compute LFs, and discuss our results.

For all calculations, we adopt a concordance cosmology with $\Omega_M = 0.3$, $\Omega_\Lambda = 0.7$, and $h = H_0/100\,\mathrm{km\,s^{-1}\,Mpc^{-1}} = 0.7$, and the AB magnitude system throughout.

2. DATA

The galaxy cluster M0416 (Ebeling et al. 2001; Mann & Ebeling 2012) lies at a redshift of $z = 0.396$ and has been extensively studied in recent years due to its inclusion in CLASH. While it does not have a particularly large critical magnification area, it contains a high number of multiply-lensed images and therefore has one of the most securely constrained mass models (e.g., Zitrin et al. 2013; Jauzac et al. 2014). M0416 is the second HFF observed cluster in *HST* cycle 21 (Figure 1). The primary *HST* observations of M0416 span dates from 2014 January 5 to September 1 (GO/DD 13496, PI: Lotz), while additional *HST* observations span dates from 2014 February 1 to September 28 (GO 13386, PI: Rodney). ACS and WFC3 images were downloaded from the Mikulski Archive for Space Telescopes (MAST[18]). Total exposure times and limiting magnitudes for each band are listed in Table 1. We processed the *HST* data with the APLUS (Zheng et al. 2012a) pipeline; for details refer to Zheng et al. (2014). The pipeline products include mosaic images, source catalogs, and photometric redshifts. To complement the *HST* data set, deep *Spitzer*/IRAC channel 1 and 2 imaging, which correspond to 3.1–3.9 and 3.9–5.0 μm, respectively, was acquired between 2013 December and 2014 March using Director's Discretionary Time (Program 90258, PI: Soifer). Additional archival data (Program 80168; PI: Bouwens) between 2011 October and 2012 April were also used. The total effective exposure time per channel is 341 ks. Images were processed with the standard *Spitzer* pipeline MOPEX (Makovoz & Khan 2005) and calibrated as described in Zheng et al. (2014).

Performing photometry on the *Spitzer*/IRAC images is challenging, as many of our candidates suffer contamination from nearby objects due to the instrument's large point-spread function (PSF, FWHM $\sim 1\farcs6$). To address this issue, we modeled all nearby objects in a 10×10 arcsec^2 region using the deep F160W band of *HST* and subtracted these objects' models from the IRAC images using GALFIT (Peng et al. 2010) to perform relatively accurate aperture photometry. We modeled the objects with point models for unresolved objects or Sérsic models for extended objects convolved with the IRAC PSF. The IRAC PSF was derived from isolated point sources that were carefully selected in the same field. The photometry of each candidate was performed with a $2\farcs5$ diameter circular aperture after the subtraction of nearby galaxies. The errors were calculated based on fluctuations in the residual image. We applied a factor of 2.0 aperture correction to account for light outside of the aperture in the wings of the PSF. During this procedure, we occasionally found candidates that (a) lay very close to nearby objects, (b) were in crowded regions with several bright galaxies, (c) straddled gaps between different exposure levels, or (d) were in regions with complex background; we flagged such candidates

[18] http://archive.stsci.edu/hst

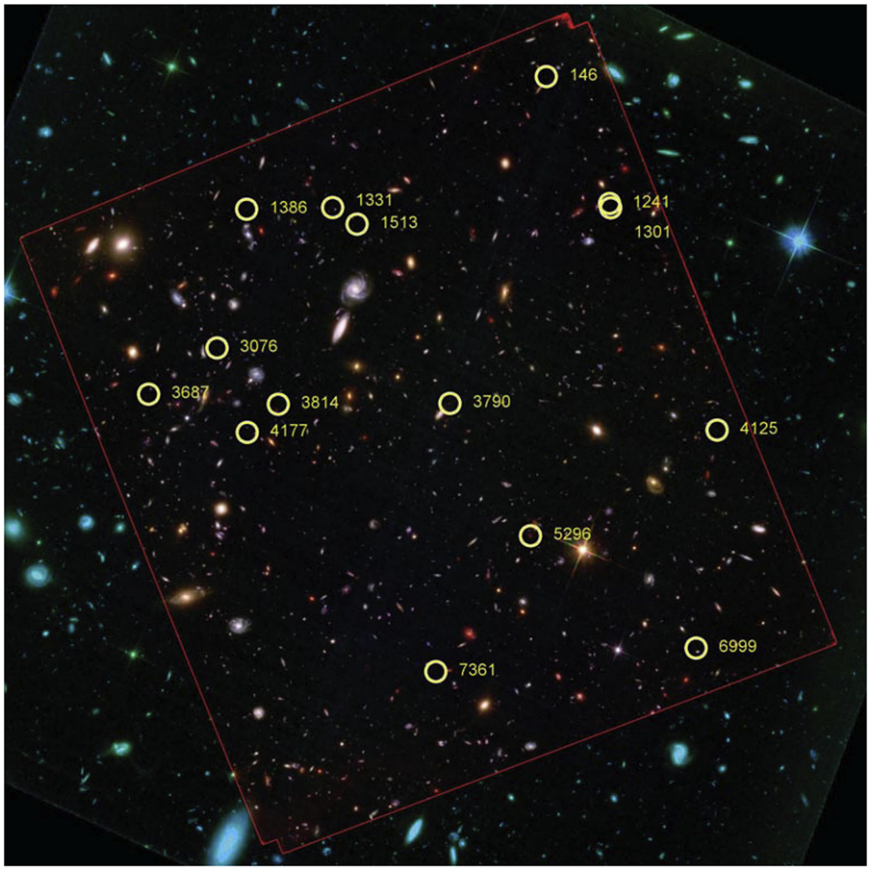

Figure 2. $3' \times 3'$ *HST* color image of the M0416 parallel field, comprising the ACS F606W (blue), ACS F814W (green), and WFC3 F160W (red) bands. Again, our $z > 7$ candidates are labeled and marked with yellow circles.

as highly contaminated. IRAC photometry for all candidates is provided in Table 2.

Parallel observations were made during the same period and with the same filters as the primary *HST* observations (Figure 2). Exposure times in these bands are listed in Table 1. The M0416 parallel field is centered at R.A. $= 04^{\rm h}16^{\rm m}33\overset{\rm s}{.}5$ decl. $= -22^\circ\,06'\,48''$. This field is also covered by the *Spitzer*/IRAC observations of M0416.

To increase the wavelength coverage of our survey and therefore increase the number of SED constraints for our candidates, we used a deep K_s image taken with HAWK-I/VLT (Pirard et al. 2004) between 2013 November and 2014 February (ID: 092.A-0472, PI: G. Brammer). The field of view of this image covers both the cluster and parallel fields. The raw HAWK-I images were processed using a custom pipeline, which was originally developed for the NEWFIRM Medium Band Survey (Whitaker et al. 2011) and later adapted for the ZFOURGE (Spitler et al. 2014) and HAWK-I Frontier Fields (G. Brammer, in preparation) surveys. We measured the image depth using empty $0\overset{''}{.}4$ radius apertures distributed over the field, resulting in a 5σ limiting magnitude of 26.1.

3. SELECTION

Candidate selection was performed using typical Lyman-break galaxy (LBG) dropout criteria, searching for LBG candidates using their distinct color around 0.1216 $(1 + z)$ μm. The criteria are as follows. For candidates at $z \simeq 7$–8, the Lyman break is at $\sim$1 μm, between the F814W and F125W bands: F814W $-$ F105W > 0.8, F105W $-$ F125W < 0.6, and F814W $-$ F105W $> 0.8 +$ (F105W $-$ F125W). These color cuts are similar to those utilized in previous work (e.g., Oesch et al. 2010; Zheng et al. 2014). For $z \simeq 8$–9, the break is at $\sim$1.15 μm, between the F105W and F140W bands: F105W $-$ F140W > 0.8, F140W $-$ F160W < 0.6, and F105W $-$ F140W $> 0.8 +$ (F140W $-$ F160W). Finally, for $z \simeq 10$, the break is between the F125W and F160W bands: F125W $-$ F160W > 0.8.

For each redshift range, a strong requisite is that a candidate should not be detected above 1σ in images bluer than the Lyman break. For $z \simeq 7$ objects, a null detection is required in the synthesized F606W and F435W band, while for candidates at $z \gtrsim 8$ a null detection is enforced in a stacked optical image.

In order to avoid contaminated photometry, we further excluded objects that fall within 1 arcsecond from the edge of the detector. We also excluded objects near stellar diffraction peaks. Finally, objects that have color decrements F160W $-$IRAC1 > 3 were eliminated, as they were most likely extremely red objects at lower redshift ($z \simeq 2$).

In addition, we corrected to the total flux using $\rm mag_{auto} - mag_{iso}$ in the F160W band, following Zheng et al. (2014). Where blending is a problem, the aperture was visually chosen so that it would not extend into the other source's lobe. Furthermore, in those cases where we used the publicly released *HST* mosaics, we verified that our aperture colors were not affected by image artifacts (e.g., Koekemoer et al. 2013).[19]

[19] http://archive.stsci.edu/pub/hlsp/frontier/macs0416/images/hst/v1.0

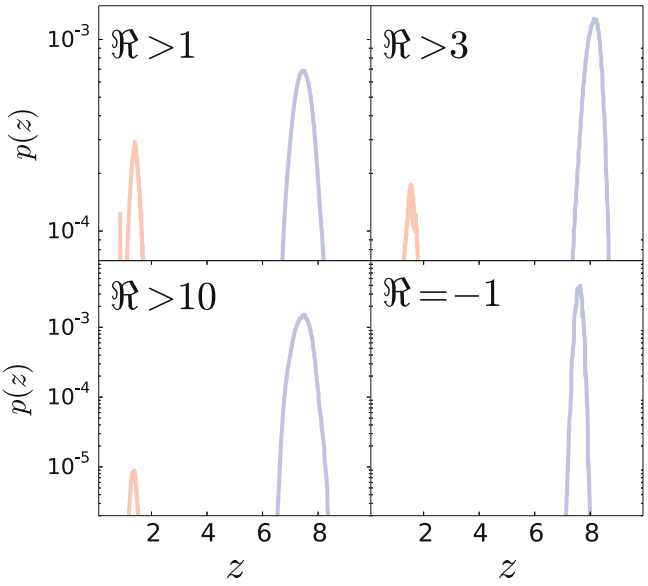

Figure 3. Color-z degeneracy problem and its separation among spectral-types. For the identification of high-z galaxies, if a sufficiently large wavelength coverage is not available or the photometry is not deep enough for the simultaneous identification of the most prominent spectral features, several solutions may equally fit the input photometric data. This problem, known as the color-z degeneracy, makes the PDF bimodal since the 4000 Å-break from an early-type galaxy at low-z cannot be distinguished from the Lyman break from a late-type galaxy at high-z. However, since this bimodality represents two independent scenarios for a single galaxy (left: early-type/low-z or right: late-type/high-z), the global PDF can be separated into two independent redshift distributions, allowing the probability comparison of both scenarios. We show four examples for $\mathcal{R} = 1, 3, 10, -1(\infty)$.

3.1. Photometric Redshift Selection

We calculate photometric redshifts (photo-z's) using an updated version of the Bayesian Photometric Redshifts code (hereafter BPZ2.0; Benítez 2000; Coe et al. 2006), which includes several changes with respect to its original version (see Molino et al. 2014 for more details). In particular, we use a new library composed of six SED templates originally drawn from Projet d'Étude des GAlaxies par Synthèse Évolutive (Fioc & Rocca-Volmerange 1997) but then re-calibrated using FIREWORKS photometry and spectroscopic redshifts (Wuyts et al. 2008) to optimize its performance. In addition to these basic six templates, four GRAphite and SILicate (*GRASIL*) and one *STARBURST* template have been added. This new library, already adopted by the CLASH collaboration (Jouvel et al. 2014), includes five templates for elliptical galaxies, two for spiral galaxies, and four for starburst galaxies, along with emission lines and dust extinction. The opacity of the IGM was applied as described in Madau (1995).

BPZ2.0 also includes a new empirically derived prior based on the redshift distributions measured in the GOODS-MUSIC (Santini et al. 2009), COSMOS (Scoville et al. 2007), and UDF (Coe et al. 2006) catalogs. However, since the galaxies considered in this work are (typically) beyond the redshift range employed to constrain the BPZ2.0 priors, we preferred to assume an ignorant (i.e., flat) prior on both galaxy type and redshift, since there is no guarantee that a simple extrapolation to the high-z universe may not introduce an unexpected bias in the analysis.

As already emphasized by several authors (Benítez 2000; Coe et al. 2006; Mandelbaum et al. 2008; Cunha et al. 2009; Wittman 2009; Bordoloi et al. 2010; Abrahamse et al. 2011; Sheldon et al. 2012; Carrasco Kind & Brunner 2013, 2014; Molino et al. 2014), photo-z's should not be treated as exact estimates, but as probability distribution functions (PDF) in a bi-dimensional (redshift versus spectral-type; i.e., z–T) space. Although it is true that for high signal-to-noise detections the PDF can be well-approximated by a Gaussian distribution, for faint detections the photometric uncertainties make these distributions highly non-Gaussian and completely asymmetric. A further difficulty arises when a sufficiently large wavelength-range coverage is not available (or the photometry is not deep enough) to simultaneously identify at least two distinct prominent spectral features (as is usually the case for the detection of very high-z galaxies), enabling more than one solution to fit the input photometric data equally well. This problem, known as the color-redshift degeneracy, makes the PDF bimodal since the 4000 Å-break from an early-type galaxy at low redshift cannot be distinguished from the Lyman break of a late-type galaxy at high-redshift. This high-to-low redshift misclassification problem is of major importance in the identification of high-z candidates.

However, since this bimodality represents two independent scenarios for a single galaxy (early-type/low-z or late-type/high-z, see Figure 3), the global PDF can be easily separated into two independent redshift distributions, as expressed in

Table 3
Photometric Redshift Estimations

ID	z^{late}_{peak}	z^{late}_{min}	z^{late}_{max}	z^{early}_{peak}	z^{early}_{min}	z^{early}_{max}	$\mathcal{R}$
M0416							
8958	10.112	9.840	10.632	2.476	2.262	10.03	4.6
1859	9.354	9.074	9.54	1.992	1.839	2.189	3.8
8364	9.234	9.049	9.294	…	…	…	−1.0*
491	8.478	8.422	8.540	…	…	…	−1.0*
8428	8.353	8.253	8.392	…	…	…	−1.0*
1213	8.311	8.138	8.392	1.483	1.428	8.052	2.2e+6
4008	7.734	7.561	7.832	1.118	0.999	1.270	2.8e+4
Parallel							
3687	9.354	8.804	9.656	2.027	2.048	9.105	4.7
4177	9.354	8.995	9.439	1.992	1.810	2.095	9.3
3076	9.002	8.837	9.249	8.807	8.697	9.03	567.5
5296	8.360	8.356	8.371	…	…	…	−1.0*
1301	8.334	8.098	8.444	1.512	1.354	1.766	783.7
3814	8.126	7.816	8.342	1.570	1.372	1.815	5.64
1241	7.939	7.738	8.133	1.399	1.301	1.519	5.8e+4
3790	7.793	7.674	7.879	…	…	…	−1.0*
4125	7.711	7.413	7.808	1.118	0.991	1.289	9.7
6999	7.634	7.489	7.695	…	…	…	−1.0*
7361	7.513	7.172	7.688	0.875	1.251	1.466	46.1
1331	7.248	7.147	7.374	0.289	0.161	0.289	8.9
1386	7.243	7.096	7.357	0.289	0.162	0.348	35.4
146	7.151	6.948	7.326	…	…	…	−1.0*
1513	7.000	6.813	7.178	1.265	1.150	1.291	1.6e+7

Notes.
[a] The table lists the photometric redshift estimations for the 22 photometrically selected candidates, where z^{late}_{peak} and z^{early}_{peak} represent the peak values for the late- and early-type spectral-solutions (respectively), z_{min} and z_{max} correspond to a 1σ confident interval, and $\mathcal{R}$ is the peak-probability ratio among solutions.
[b] Asterisked ratios (*) correspond to detections without low-redshift solutions.

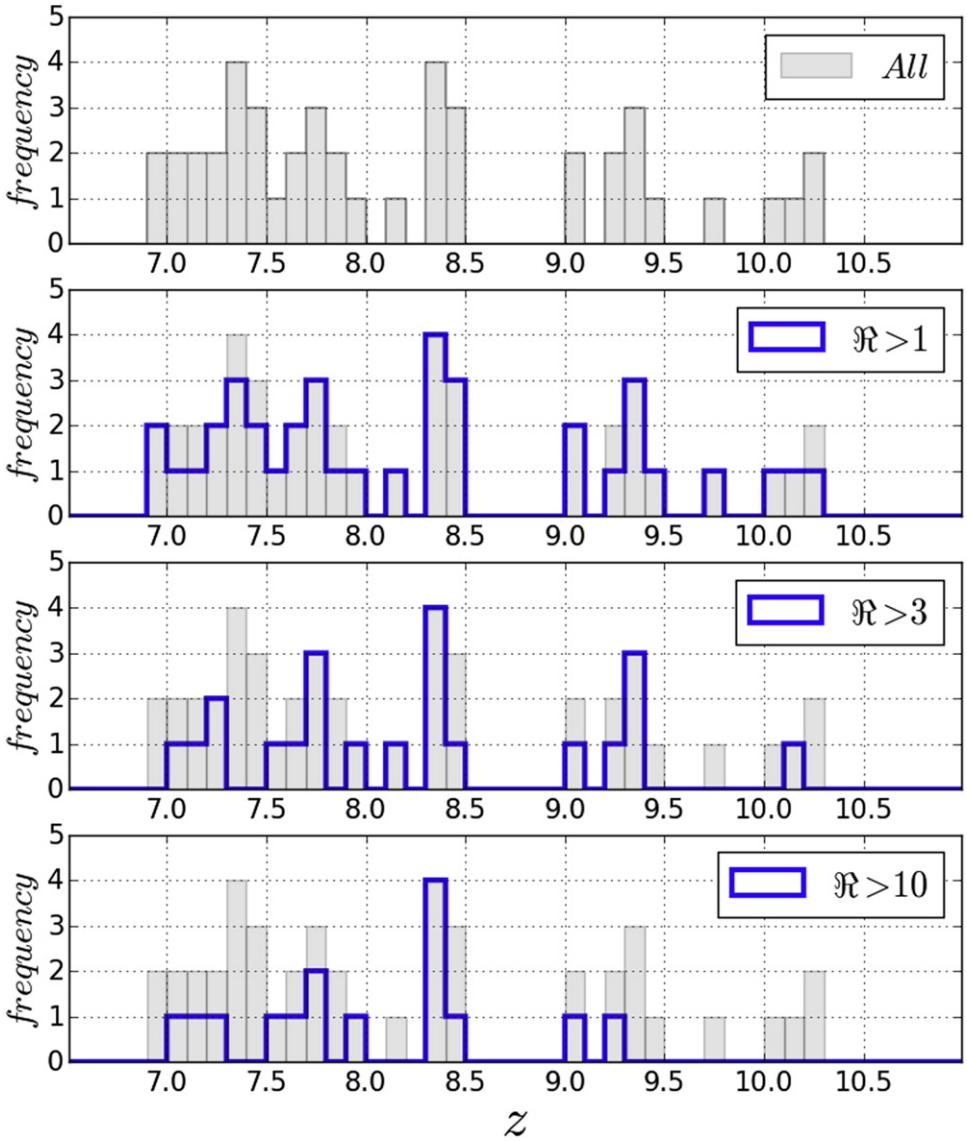

Figure 4. Distribution of peak photometric redshifts for the entire sample of $z > 7$ candidates from the M0416 cluster and parallel fields. Once the global PDF is separated among spectral-type solutions, we define the peak-probability ratio ($\mathcal{R}$) as the ratio among peak probabilities, i.e., between the values that each distribution takes in its peak (or maximum). This number roughly quantifies how many times one solution is more likely than the other, and thus allows one to flag potential $z \gtrsim 7$ candidates. The first panel shows the distribution for the entire sample of 45 photometrically selected galaxies. From these, a total of 15 "potential" candidates have a minimum threshold of $\mathcal{R} > 10$, 22 candidates have $\mathcal{R} > 3$, and 38 candidates have $\mathcal{R} > 1$. $\mathcal{R} > 3$ photometric redshifts are used in our analysis.

Equation (1):

$$p(z) = \int p(z, T)\, dT = \int p(z, T_E)\, dT + \int p(z, T_L)\, dT. \quad (1)$$

This simple separation between "red" templates (T_E) and "blue" templates (T_L) renders it possible to make simple comparisons between both scenarios. Following the same philosophy used by López-Sanjuan et al. (2015), we express the normalized global PDF for every galaxy in terms of the probability of having an early (p_E) or a late (p_L) spectral-type solution, as indicated in Equation (2):

$$P(z) = \int p(z)\, dz = p_E(z) + p_L(z) = 1. \quad (2)$$

Likewise, we define (Equation (3)) the peak-probability ratio $\mathcal{R}$ as the ratio between peak-probabilities, i.e., between the values that each distribution takes as its peak (or maximum), such that:

$$\mathcal{R} \equiv \frac{p_L(z = z_{\mathrm{peak},L})}{p_E(z = z_{\mathrm{peak},E})}. \quad (3)$$

This number approximates how many times one solution is more likely than the other and so makes possible to quantitatively flag potential high-z candidates. As shown in Table 3, where both the photometric redshift estimations and the peak-probability ratios are presented for every photometrically selected candidate, we find a total of 15 "potential" candidates lie at $z \gtrsim 7$ if we impose a minimum threshold of $\mathcal{R} > 10$. If this condition is relaxed to $\mathcal{R} > 3$ or $\mathcal{R} > 1$, we obtain 22 and 38 candidates, respectively. The resulting redshift distribution (when applying the different threshold criteria) is shown in Figure 4. To be on the conservative side, we consider as high probability only those high-redshift

Table 4
$z > 7$ Candidates and Their Properties: M0416 Field

Name	Photometric Redshift	R.A. (J2000)	Decl. (J2000)	F160W[a]	F140W[a]	F125W[a]	F105W[a]	F814W[a]	K_s[b]	μ[c]
8958	10.112	64.025406	−24.082251	28.50 ± 0.11	28.99 ± 0.17	>30.40	31.86 ± 1.92	>30.70	>27.03	20.50 ± 13.30
1859	9.354	64.043114	−24.057899	27.72 ± 0.07	27.93 ± 0.09	28.63 ± 0.18	30.53 ± 0.79	30.14 ± 0.56	27.21 ± 0.42	4.41 ± 2.44
8364	9.234	64.048058	−24.081429	26.45 ± 0.03	26.62 ± 0.04	27.07 ± 0.06	29.99 ± 0.56	>30.70	26.52 ± 0.22	1.80 ± 0.47
491	8.478	64.039169	−24.093187	25.92 ± 0.02	25.99 ± 0.03	26.41 ± 0.04	27.90 ± 0.10	28.96 ± 0.34	26.40 ± 0.20	1.71 ± 0.47
8428	8.353	64.047981	−24.081665	26.59 ± 0.03	26.59 ± 0.03	26.73 ± 0.04	28.19 ± 0.10	>30.70	>27.54	1.79 ± 0.46
1213	8.311	64.037582	−24.088104	28.12 ± 0.08	27.80 ± 0.07	27.95 ± 0.08	29.51 ± 0.25	33.03 ± 7.60	>27.46	2.36 ± 1.01
4008	7.734	64.060333	−24.064960	27.85 ± 0.08	27.86 ± 0.09	27.53 ± 0.07	28.48 ± 0.11	31.47 ± 1.57	>27.54	2.17 ± 0.31

Notes.
[a] Magnitudes are isophotal, scaled by an aperture correction term derived in the F160W band. The errors and limiting magnitudes are 1σ. Photometric redshifts have been derived using BPZ2.0.
[b] Photometry within a $0\farcs4$ radius aperture.
[c] See Section 4 for magnification factors and errors.

Table 5
$z > 7$ Candidates and Their Properties: M0416 Parallel Field

Name	Photometric Redshift	R.A. (J2000)	Decl. (J2000)	F160W[a]	F140W[a]	F125W[a]	F105W[a]	F814W[a]	K_s[b]
3687	9.354	64.156128	−24.111143	28.84 ± 0.14	29.19 ± 0.19	29.63 ± 0.32	>31.30	32.37 ± 4.17	27.78 ± 0.71
4177	9.354	64.149864	−24.113352	27.56 ± 0.06	27.61 ± 0.06	28.44 ± 0.15	29.65 ± 0.38	31.81 ± 3.82	>28.35
3076	9.002	64.151779	−24.108454	27.84 ± 0.07	27.95 ± 0.08	28.39 ± 0.14	>31.30	>31.40	>28.08
5296	8.360	64.131889	−24.119350	24.18 ± 0.01	24.49 ± 0.01	24.99 ± 0.02	26.19 ± 0.04	>31.40	24.03 ± 0.03
1301	8.334	64.126785	−24.100315	28.23 ± 0.08	28.10 ± 0.07	28.30 ± 0.09	29.69 ± 0.27	30.21 ± 0.67	>28.70
3814	8.126	64.147903	−24.111727	28.12 ± 0.08	28.19 ± 0.09	28.34 ± 0.12	29.56 ± 0.29	31.29 ± 1.93	26.74 ± 0.27
1241	7.939	64.126862	−24.100067	28.15 ± 0.07	27.89 ± 0.06	28.10 ± 0.08	29.03 ± 0.15	>31.40	>28.03
3790	7.793	64.136993	−24.111664	26.40 ± 0.03	26.54 ± 0.03	26.69 ± 0.04	27.61 ± 0.08	>31.40	>27.74
4125	7.711	64.120026	−24.113226	27.82 ± 0.06	27.89 ± 0.07	27.80 ± 0.07	28.60 ± 0.12	29.85 ± 0.47	>28.19
6999	7.634	64.121368	−24.125864	27.33 ± 0.04	27.40 ± 0.05	27.22 ± 0.04	27.94 ± 0.07	>31.40	>28.30
7361	7.513	64.137886	−24.127241	28.22 ± 0.08	28.07 ± 0.07	28.34 ± 0.11	28.89 ± 0.14	>31.40	>28.50
1331	7.248	64.144447	−24.100300	27.37 ± 0.05	27.35 ± 0.05	27.24 ± 0.05	27.68 ± 0.06	29.38 ± 0.39	>28.06
1386	7.243	64.149895	−24.100410	27.82 ± 0.06	27.62 ± 0.05	27.66 ± 0.06	28.04 ± 0.06	31.21 ± 1.51	>28.32
146	7.151	64.130882	−24.092710	27.58 ± 0.06	27.50 ± 0.05	27.72 ± 0.07	27.99 ± 0.07	>31.40	>28.19
1513	7.000	64.142899	−24.101274	28.14 ± 0.08	28.12 ± 0.08	28.02 ± 0.08	28.30 ± 0.09	>31.40	>28.58

Notes.
[a] Magnitudes are isophotal, scaled by an aperture correction term derived in the F160W band. The errors and limiting magnitudes are 1σ. Photometric redshifts have been derived using BPZ2.0.
[b] Photometry within a $0\farcs4$ radius aperture.

candidates with $\mathcal{R} > 3$. Moreover, it is interesting to note that the use of $\mathcal{R} > 3$ instead of $\mathcal{R} > 1$ suggests a contamination rate of ≈40%, on the order of what was found in previous surveys (e.g., Bradley et al. 2012; Schmidt et al. 2014). We know the peak ratio $\mathcal{R}$ is probably not the best estimate; it is just the simplest and good enough for our purpose.

In Tables 4–5 we present identifications, positions, and photometry for all our selected candidates with $\mathcal{R} > 3$. In Figures 5–7, we show cutout images of all the $\mathcal{R} > 3$ candidates. In the discussion that follows we only consider these candidates and use these BPZ based redshifts for all further calculations, e.g., LF, physical properties, etc.

4. LENS MODELS

We derive magnifications for the different candidates from a selection of lens models publicly available through the MAST archive.[20] In order to maintain consistency among these models, we select only those that incorporate the cluster members into the lens model.

In particular, we use the two models delivered by the Sharon team (Johnson et al. 2014), the two models delivered by the Zitrin & Merten team (Zitrin et al. 2013), and one model delivered by the CATS team (Richard et al. 2014). In addition to these five models, we also include the free-form model from Diego et al. (2015) which, like the models above, includes the contribution from cluster members to the lens model.

Based on these six models we compute the mean magnifications at the corresponding redshifts for the candidates listed in Table 4 as well as the dispersion in the magnification between the different models. The candidates that are further away from the critical curves show smaller dispersion between the predicted magnification values. The critical curves for one of these models (Diego et al. 2015) together with the position of the candidates around the central part of the cluster are shown in Figure 1.

[20] http://archive.stsci.edu/prepds/frontier/lensmodels/

For candidates near the critical curves, we use the model to predict potential counter images. Variations in the predictions of counter images are expected between different models especially near the critical curves. For candidate 8958 we find that the models predict two additional counter images. The precise location varies depending on the particular model but with a fair agreement between different models. Based on the Diego et al. (2015) model, counter images should be found at (a) R.A. = 64.°023524, decl. = −24.°07943 ($\mu = 3.9$) and at (b) R.A. = 64.°036003, decl. = −24.°08669 ($\mu = 1.7$). At both positions, we locate several faint red objects within 2 arcsec of the predicted position. In particular, for predicted position (a) we find three faint candidates within 1.5 arcsec and for predicted position (b) we find one candidate ≈1.8 arcsec away. However, despite the presence of possible candidates around the predicted positions, we note that the relatively weaker magnification at the predicted positions compared with the large magnification for the already faint candidate 8958 ($\mu \approx 20$) makes it difficult to reach a reliable identification of candidates at the predicted positions.

5. DISCUSSION

5.1. Contamination

One possible source of contamination of the high-z sample is from low-z interlopers (e.g., Hayes et al. 2012) that could fulfill all the selection criteria defined for very high-redshift objects. We estimated the contamination by this type of source by simulating a population of galaxies based on the distribution of galaxies in our data set. We first build this "contaminant sample" by selecting all objects that are brighter than the brightest candidate selected in the field (F160W > 25.5) and that are detected at more than 2σ in optical bands (for the parallel field we used the same limit even though we selected one object at F160W = 24.18; see discussion below). We then matched the luminosity distribution of the bright objects to the luminosity of our candidates. We measured the noise around each object to update the photometry of the contaminants' sample. Finally we applied the same selection criteria as those

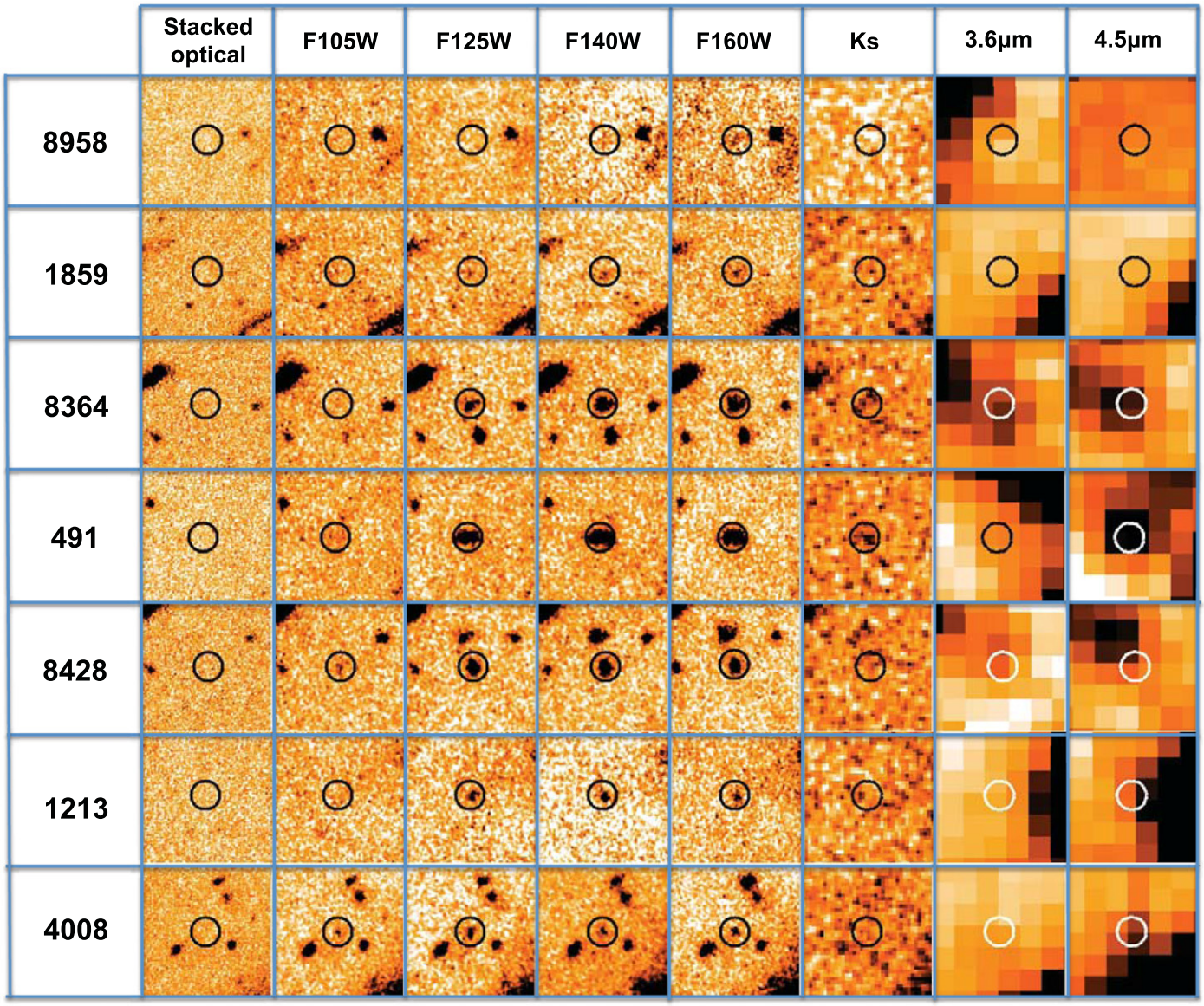

Figure 5. Postage stamp images for all $z > 7$ candidates in the M0416 cluster field. The stamp size is $4'' \times 4''$ and the radius of the circle is $0\farcs4$.

we used for the high-z selection: all the objects that enter the selection window are contaminants. As a first step, we only applied the classical LBG selection criteria (non-detection and color selection) and found a contamination rate of ∼28% for the cluster sample and ∼42% for the parallel sample. We then applied to the selected contaminants the peak probability ratio method and found that all the objects in the contaminants sample display a ratio $R < 2$, such that they are not selected as good candidates.

Moreover, the high-z sample can also be contaminated by M, L, and T dwarfs exhibiting colors similar to what are required for high-z galaxies. We used observed spectra of such stars published in Burgasser et al. (2004, 2010) and showed that this kind of contaminant has the following colors: F105W–F140W < 1.0 and F140W–F160W < 0.4. Therefore, among our samples, nine objects are consistent with these colors and require further investigation. We measured the size of these nine objects following the method described in Oesch et al. (2010), correcting for PSF broadening and amplification, and demonstrated that all nine objects are resolved on *HST* images.

5.2. The Brightest $z \sim 8$ Candidate

Among our two samples, one $z \sim 8$ candidate appears extremely bright (F140W ∼ 25.5) without being strongly amplified because it is located in the parallel field (#5296). The expected number of such bright objects in the full Frontier Fields data set (∼32 arcmin^2 according to Coe et al. 2015) assuming the evolution of the UV LF found by Bouwens et al. (2015) is $(1.33^{+5.00}_{-0.96}) \times 10^{-3}$. We also note that only one object with F140W < 24.5 is expected in the final release of the UltraVISTA survey (MacCracken et al. 2012), implying that a high-redshift hypothesis is unlikely. In order to assess whether this extreme object is an interloper or a bona fide high-redshift galaxy, we perform several tests.

We first study the non-detection in the optical bands by applying the $\chi^2_{\rm opt}$ method defined in Bouwens et al. (2011b). We compare the distribution of $\chi^2_{\rm opt}$ measured in empty apertures all over the field with the distribution of $\chi^2_{\rm opt}$ for mock objects detected at ∼2σ in all ACS bands and show that all

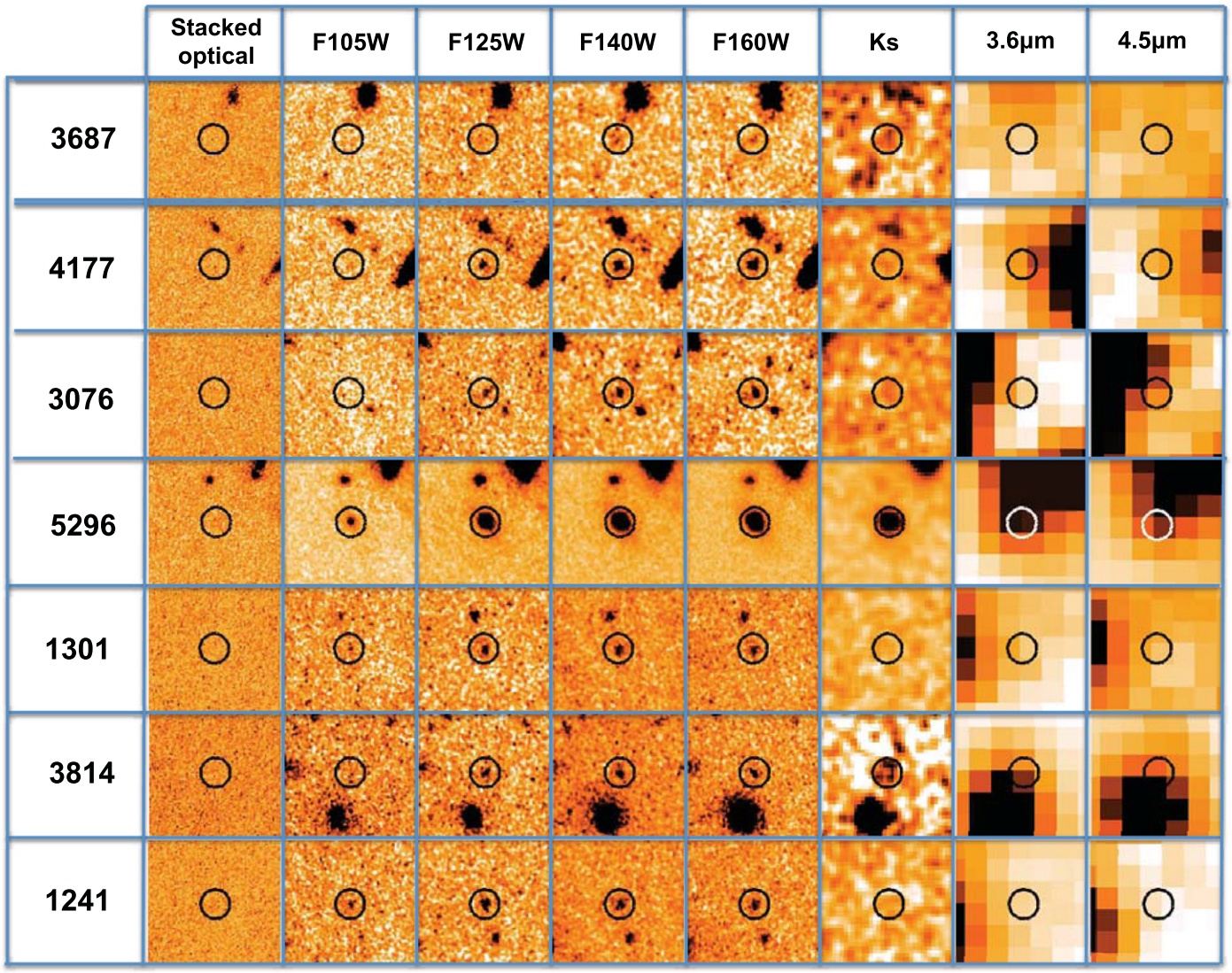

Figure 6. Postage stamp images for all $z > 7$ candidates in the M0416 parallel field, part 1. Details are the same as in Figure 5.

sources with $\chi^2_{\rm opt} > 0.4$ are most likely contaminants. The $\chi^2_{\rm opt}$ of our source is in perfect agreement with the $\chi^2_{\rm opt}$ measured in empty apertures [$\chi^2_{\rm opt}(\#5296) = -0.04$]. However, we notice a possible faint detection of that object on the F814W image (>30.1) that could make the $z \sim 8$ hypothesis unlikely, but that confirms a huge break between optical and NIR data of at least 4.5 mag.

The star hypothesis was studied by measuring the size of this object and by comparing its colors with expected colors of M, L, and T dwarfs, which could be similar to those of very high-z objects. We measured its size using the SExtractor FLUX_RADIUS parameter which encloses 50% of the light, as described in Oesch et al. (2010), and corrected this value for PSF broadening. This shows that this object is clearly resolved, and assuming that this object is at $z \sim 8.36$, its physical size would be 0.55 kpc, which is consistent with the observed evolution of size as a function of UV luminosity (e.g., Kawamata et al. 2015; Laporte et al. 2015). As in Section 5.1, we compared the colors of this candidate (F105W–F140W = 1.7 and F140W–F160W = 0.31) to those expected from M, L, and T dwarfs (F105W–F140W < 1.0 and F140W–F160W < 0.4), finding that they are incompatible.

The last hypothesis we study for this target is the possibility that it is a moving object. We took benefit from the 4 epochs during which the parallel field has been observed with WFC3/*HST*, which span over 1 month. We ran SExtractor on each epoch image and compared the centroid position for that object; it shows no evidence of movement.

5.3. Physical Properties

Next, we characterize the physical properties of our high-redshift candidates by means of the Bayesian SED modeling code `iSEDfit` (Moustakas et al. 2013). Using the same setup and parameter set as used in Zheng et al. (2014), we generated 80,000 model SEDs with *delayed* star formation histories using a Monte Carlo technique. iSEDfit also includes nebular emission lines. The SEDs were computed employing the Flexible Stellar Population Synthesis models (FSPS, v 2.4; Conroy et al. 2009; Conroy & Gunn 2010) based on the MILES (Sanchez-Blázquez et al. 2006) and Basel (Lejeune et al. 1997, 1998; Westera et al. 2002) stellar libraries, and assume a Chabrier (2003) initial mass function from 0.1 to 100 $M_\odot$.

We adopt uniform priors on stellar metallicity $Z/Z_\odot \in [0.04, 1.0]$, galaxy age $t \in [0.01, {\rm age}(z_{\rm BPZ})]$ Gyr,

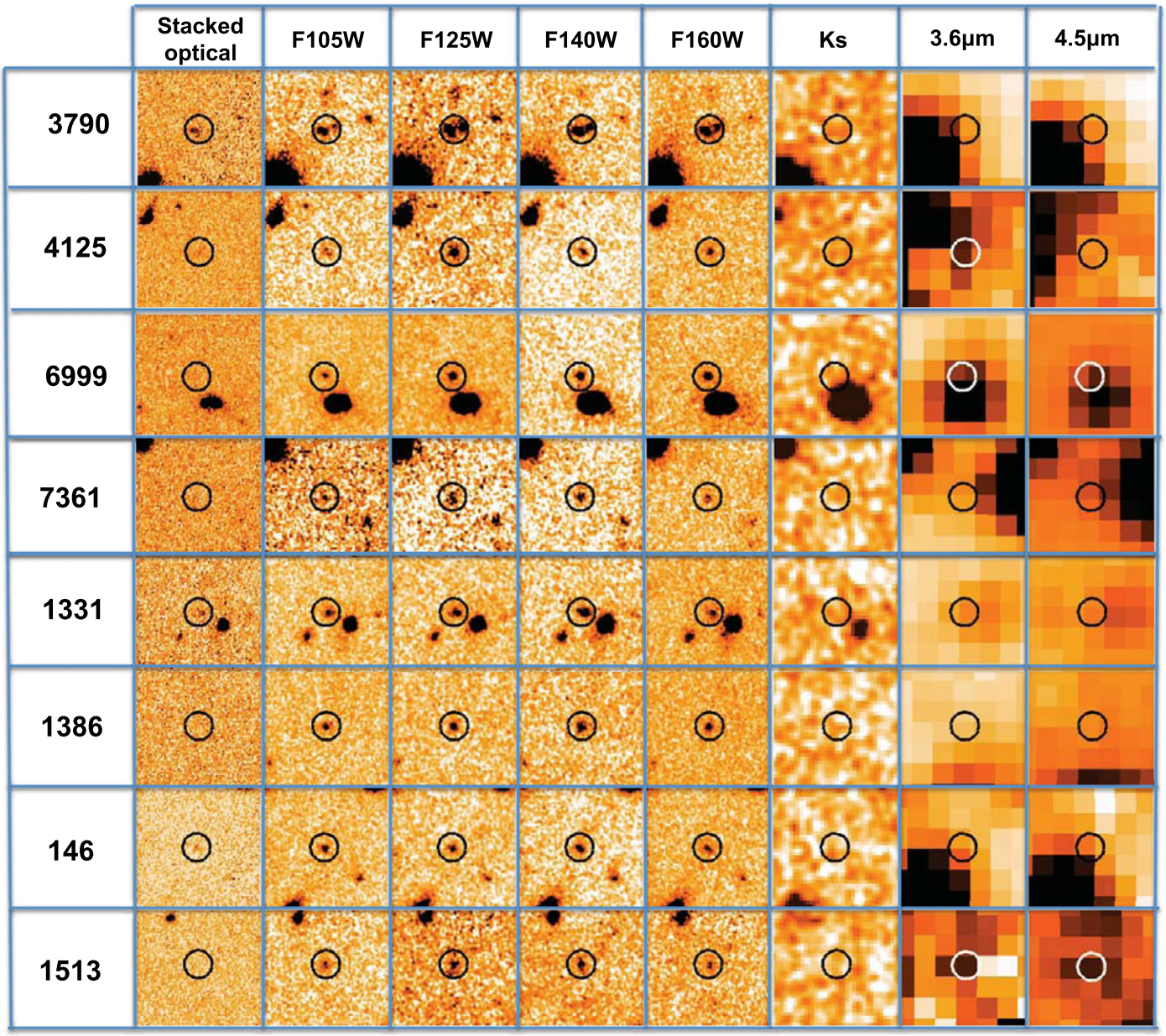

Figure 7. Postage stamp images for all $z > 7$ candidates in the M0416 parallel field, part 2. Details are the same as in Figure 5.

star formation timescale $\tau \in [0.01, \mathrm{age}(z_{\mathrm{BPZ}})]$ Gyr, where age (z_{BPZ}) is the age of the universe at each galaxy's photometric redshift, and we assume no dust attenuation (e.g., Bouwens et al. 2010). In Table 6 we report the median values of the posterior probability distributions for some physical properties and their 1-σ confidence level uncertainties. Our $z > 7$ candidates have median stellar masses of $\log(M_*) \sim 8.44^{+0.55}_{-0.31}\,M_\odot$, star formation rates (SFRs) of approximately $1.8^{+0.5}_{-0.4}\,M_\odot\ \mathrm{yr}^{-1}$, and SFR-weighted ages of $\lesssim 300^{+70}_{-140}$ Myr.

Figures 8 and 9 present the SEDs of the high-z candidates in the M0416 cluster and parallel fields, sorted by decreasing redshift.

In order to evaluate the validity of the "no dust" condition adopted above, we also create 40,000 models employing the time-dependent attenuation curve of Charlot & Fall (2000) and rest-frame V-band attenuations of $A_V \in [0 - 3]$ mag. We note that our SEDs are generally best-fitted with the models having little or no dust attenuation, obtaining a median A_V of $0.28^{+0.16}_{-0.23}$ mag, and a similar median stellar mass [$\log(M_*) \sim 8.53^{+0.36}_{-0.29}$ and age $\sim 210^{+60}_{-130}$ Myr] as those reported previously without considering dust attenuation. Yet, dust has a big impact on the SFRs; its median value increases by a factor of two from $1.8^{+0.5}_{-0.4}$ to $\sim 3.5^{+0.5}_{-0.2}\,M_\odot\ \mathrm{yr}^{-1}$. The reported median values are based on the median values of each posterior probability distribution.

Finally, since the physical-property estimation depends on the photometric redshift assumption, we also use `iSEDfit` to calculate photometric redshifts. The comparison of these results allow us to evaluate how reliable is our estimation of the physical properties based on BPZ redshifts. We generate 40,000 SEDs models adopting the same SSP models, stellar libraries, parameterization of the star formation history, and IMF as used in the previous calculation of the physical

Table 6
Physical Properties of the Candidates Inferred from Their SEDs

Galaxy ID	Redshift	log M_* ($M_\odot$)	log SFR ($M_\odot$ yr^{-1})	AGE (Gyr)
M0416				
8958	10.112	$8.92^{+0.50}_{-0.29}$	$-0.13^{+0.13}_{-0.60}$	$0.33^{+0.09}_{-0.13}$
1859	9.354	$8.52^{+0.28}_{-0.43}$	$0.37^{+0.09}_{-0.08}$	$0.25^{+0.17}_{-0.17}$
8364	9.234	$9.15^{+0.28}_{-0.37}$	$0.86^{+0.07}_{-0.09}$	$0.32^{+0.14}_{-0.17}$
491	8.478	$9.49^{+0.17}_{-0.22}$	$0.95^{+0.07}_{-0.13}$	$0.40^{+0.13}_{-0.16}$
8428	8.353	$9.12^{+0.26}_{-0.31}$	$0.73^{+0.06}_{-0.10}$	$0.38^{+0.15}_{-0.18}$
1213	8.311	$8.40^{+0.30}_{-0.42}$	$0.22^{+0.08}_{-0.08}$	$0.29^{+0.20}_{-0.19}$
4008	7.734	$8.44^{+0.32}_{-0.44}$	$0.26^{+0.09}_{-0.08}$	$0.30^{+0.23}_{-0.21}$
Parallel				
3687	9.354	$8.05^{+0.33}_{-0.46}$	$-0.10^{+0.10}_{-0.10}$	$0.25^{+0.17}_{-0.17}$
4177	9.354	$8.59^{+0.31}_{-0.42}$	$0.46^{+0.09}_{-0.08}$	$0.25^{+0.17}_{-0.16}$
3076	9.002	$8.34^{+0.22}_{-0.34}$	$0.29^{+0.08}_{-0.07}$	$0.22^{+0.16}_{-0.13}$
5296	8.360	$11.02^{+0.04}_{-0.04}$	$0.99^{+0.18}_{-0.40}$	$0.34^{+0.15}_{-0.11}$
5296	6.901	$11.04^{+0.01}_{-0.01}$	$-3.83^{+0.24}_{-0.24}$	$0.27^{+0.02}_{-0.02}$
1301	8.334	$8.31^{+0.29}_{-0.42}$	$0.13^{+0.08}_{-0.08}$	$0.28^{+0.20}_{-0.18}$
3814	8.126	$8.38^{+0.30}_{-0.40}$	$0.08^{+0.08}_{-0.10}$	$0.33^{+0.19}_{-0.20}$
1241	7.939	$8.37^{+0.27}_{-0.39}$	$0.14^{+0.08}_{-0.08}$	$0.31^{+0.20}_{-0.19}$
3790	7.793	$8.67^{+0.09}_{-0.14}$	$0.77^{+0.04}_{-0.06}$	$0.16^{+0.07}_{-0.06}$
4125	7.711	$8.58^{+0.38}_{-0.41}$	$0.20^{+0.08}_{-0.12}$	$0.39^{+0.19}_{-0.23}$
6999	7.634	$8.29^{+0.19}_{-0.31}$	$0.47^{+0.08}_{-0.06}$	$0.14^{+0.12}_{-0.09}$
7361	7.513	$8.36^{+0.29}_{-0.40}$	$0.04^{+0.08}_{-0.09}$	$0.37^{+0.21}_{-0.22}$
1331	7.248	$7.52^{+0.10}_{-0.06}$	$0.83^{+0.19}_{-0.13}$	$0.01^{+0.01}_{-0.00}$
1386	7.243	$8.49^{+0.27}_{-0.38}$	$0.22^{+0.08}_{-0.08}$	$0.35^{+0.23}_{-0.21}$
146	7.151	$8.08^{+0.16}_{-0.27}$	$0.33^{+0.07}_{-0.06}$	$0.12^{+0.09}_{-0.07}$
1513	7.000	$8.47^{+0.38}_{-0.43}$	$0.03^{+0.09}_{-0.11}$	$0.44^{+0.22}_{-0.26}$

Note. The following quantities are reported in each column: col. 1, object name; col. 2, object redshift; col. 3, logarithm of the stellar mass inferred by using the FSPS-v2.4 miles; col. 4, star formation rate; col. 5, galaxy age. Values corrected by their magnification factor. Errors are shown at the 1σ confidence level.

properties including dust (Charlot & Fall 2000 curve and $A_V \in [0-3]$ mag). Nevertheless, in order to additionally encompass possible low-redshift interlopers, we model these SEDs within a broader range of uniform priors on age $t \in [0.01, 13.5]$ Gyr, star formation timescale $\tau \in [0.01, 5.0]$ Gyr, stellar metallicity $Z/Z_\odot \in [0.04, 1.6]$ than used previously. Despite the fact that iSEDfit was optimized to estimate the physical properties and not photometric redshifts, we note that the photo-z's obtained with iSEDfit and BPZ2.0 are reassuringly similar. iSEDfit tends to recover slightly higher photo-z's compared to BPZ2.0, although the values are consistent within the error bars, yielding a mean difference of $\Delta z = 0.1 \pm 0.1$ (iSEDfit minus BPZ2.0). Since there are no substantial differences between the photo-z's based on BPZ and iSEDfit, except for the candidate 5296, we can rely on the physical properties' estimation based on the BPZ redshift. It excludes the outlier high-redshift candidate 5296, where both photometric redshifts clearly differ, z(BPZ2.0) $= 8.360^{+0.011}_{-0.004}$ and z(iSEDfit) $= 6.9 \pm 0.4$. Hence in Table 6, we report the physical properties according both photometric redshifts for this particular candidate.

These physical properties agree with the results of Schaerer & de Barros (2010). The relatively small size of our sample and its faintness does not allow us to draw a firm conclusion that a star-forming main-sequence is in place at $z > 6$. Nevertheless, we do confirm that our candidates conform to the reddening-stellar-mass plane proposed by Schaerer & de Barros (2010): $A_V = \log_{10}(M/10^8\,M_\odot)^n$ with $n = 0.4$–0.7.

5.4. Number Densities at $z \sim 7$, 8, 9, and 10

The deep images obtained from Frontier Fields observations and the amplification of the light coming from background sources by the cluster enable us to probe a large range in intrinsic luminosities, thereby allowing us to constrain the UV LF to unprecedentedly faint levels. We use the two samples selected in the cluster and parallel fields to compute the number densities in the redshift range covered by our survey. We apply a Monte Carlo method based on the redshift probability distribution (Laporte et al. 2015). We summarize the eight steps we use to estimate the shape of the UV LF:

1. For each object in our samples, we compute the cumulative redshift probability distribution, $P_{\rm cum}(z)$.
2. We choose a random probability, a, that assigns a redshift, z_a, for each object from the cumulative redshift probability distribution such that $P_{\rm cum}(z_a) = a$.
3. We use this redshift and the SED of each object to estimate its UV luminosity corrected for amplification.
4. Steps 1 and 2 are repeated N times in order to get a sample with N times the size of the original sample, but with the same redshift distribution. We adopt a value N large enough so as to not affect the final result (in our case $N = 10{,}000$).
5. We distribute all the objects with a redshift included between $z - 0.5$ and $z + 0.5$, where $z = 7$, 8, 9, or 10, in magnitude bins and correct each object for incompleteness.
6. Each number is corrected by the contamination rate.
7. We compute the effective surface explored by the M0416 data set by matching the amplification map with the detection picture, and then divide the number of objects per magnitude bin by the comoving volume explored between $z - 0.5$ and $z + 0.5$, where $z = 7$, 8, 9, or 10.
8. Uncertainties on each density are computed using the method described in Trenti & Stiavelli (2008).

The number densities are then corrected for incompleteness due to the extraction methods and the selection criteria we apply to catalogs. The selection function we use to build our high-z samples involves the "standard" Lyman break technique (Steidel et al. 1999) and the use of the $P(z)$ ration between early-type and late-type galaxies. Therefore we divided the completeness of our sample into two parts, corresponding to each selection criteria we used, as follows:

$$C_{\rm LBt}(m, z) \times C_{\rm pic}(m, z). \quad (4)$$

The first part of the previous equation, $C_{\rm LBt}(m, z)$, is the incompleteness due to the Lyman break technique and more especially to the extraction method and color criteria we used. To estimate the shape of this function, we simulate 680,000 galaxies from the latest Starburst99 library (Leitherer et al. 1999; Vázquez & Leitherer 2005; Leitherer et al. 2010; Leitherer et al. 2014) and other theoretical templates (Coleman et al. 1980; Kinney et al. 1996; Silva et al. 1998; Bruzual & Charlot 2003; Polletta et al. 2007). The space parameters we

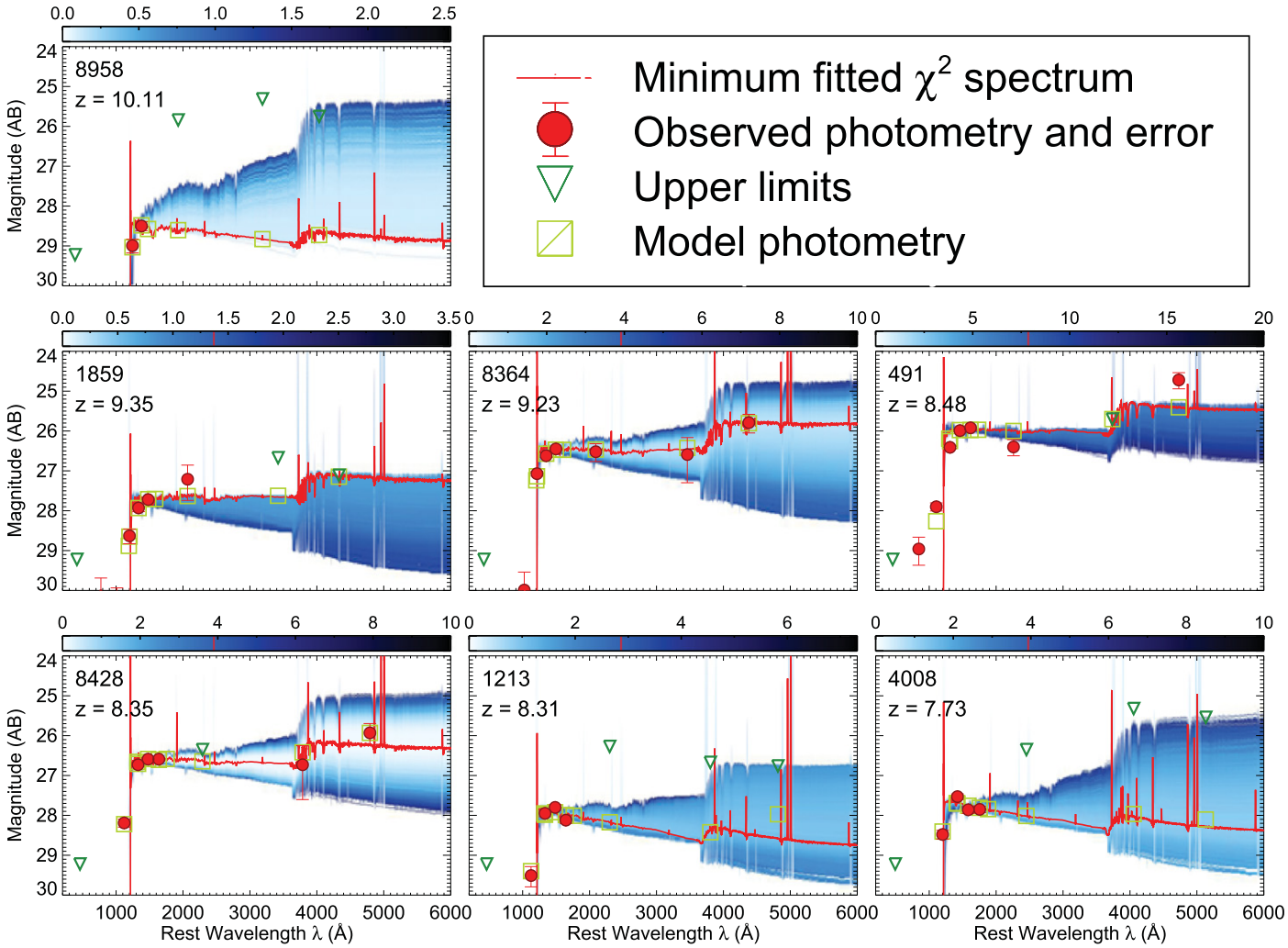

Figure 8. Rest-frame SEDs of the $z \geqslant 7$ candidates in the M0416 cluster field. Filled red circles denote observed ACS, WFC3, HAWK-I/VLT, and IRAC photometric detections, while open green triangles indicate 3σ upper limits. The red spectrum shows the best-fitting (maximum likelihood) SED template based on our Bayesian SED modeling using `iSEDfit`. The large green squares show the expected photometric magnitudes of the best-fitting model convolved with the ACS, WFC3, and IRAC filter response curves. The blue shading shows some models, which were used in the fitting process, scaled by their χ^2. The color bar shows the χ^2 scale.

used had magnitudes ranging from 22.00 to 31.00 and redshifts from 6.5 to 10.5. We then defined an object mask from the detection picture to identify positions where no object is detected and then added the simulated objects to the real data without masked objects. We assumed a log-normal distribution of the size of very high-redshift objects with a mean value of $0\farcs15$ and a sigma of $0\farcs07$ as expected from previous studies (e.g., Oesch et al. 2010). We then used the same extraction software and selection criteria as defined in Section 3 and compared the number of extracted objects with the number of simulated objects.

The second part of Equation (4), $C_{\rm pic}(m, z)$, is computed from a mock catalog containing ≈50,000 objects with redshift ranging from 0 to 12 and a luminosity distribution matched to the $z \sim 6$ LF published in Bouwens et al. (2015). We run BPZ2.0 and computed for each object the ratio between the probability of this object being an early-type (low-z) galaxy and the probability of it being a late-type (high-z) galaxy. The completeness is computed by applying the $P(z)$ selection criteria to this mock catalog and by comparing the selected sample with the number of high-z simulated objects.

The number densities we found are reported in Table 7. It is interesting to note that one object at $z \sim 10$ is strongly amplified ($\mu \sim 20$) and thus allows us to give for the first time a robust constraint in the faint end ($L \sim 0.04\ L^*$) of the UV LF at $z \sim 10$. This result is consistent with the shape of the LF observed at the brightest luminosities at such high redshifts.

Recently several papers have demonstrated that the role of foreground galaxies in the amplification of the light coming from very high-redshift objects is negligible (<1%) for objects selected in *HST* surveys (e.g., Fialkov & Loeb 2015). Therefore we only corrected photometry for lensing by galaxy clusters in both fields.

One also has to bear in mind that lensing itself introduces incompleteness to the reconstructed LF. While the so-called magnification bias (Broadhurst et al. 1995), which preferentially biases toward the detection of more magnified objects in lensed fields, is effectively folded in our derivation of the LF, there are other lensing-related biases that need to be addressed. For example, Oesch et al. (2014) have shown that both shear (or the apparent change in shape of lensed images) and source blending, have a noticeable effect on the reconstructed LF, biasing the derived SFRD by order 0.4

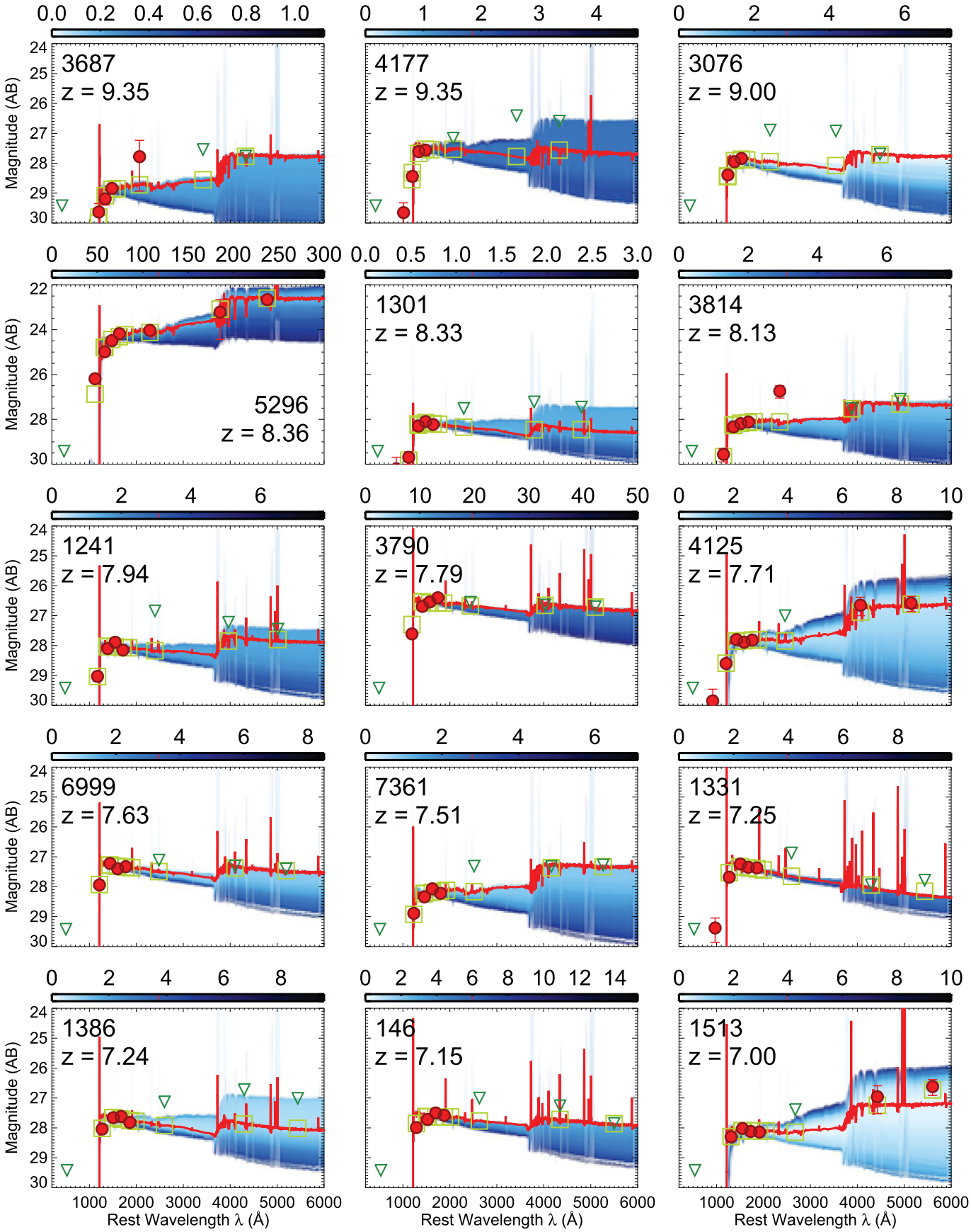

Figure 9. Rest-frame SEDs of $z \geqslant 7$ candidates in the parallel field. Details are the same as Figure 8.

Table 7
Number Densities at $z \sim 7$, 8, 9, and 10

Redshift Range	M_{1500}	$\Phi(M_{1500})$ [/Mpc^3/mag]
$z \sim 7$	-20.75 ± 0.500	$(1.64 \pm 1.37) \times 10^{-04}$
	-19.75 ± 0.500	$(3.72 \pm 2.32) \times 10^{-04}$
	-18.75 ± 0.500	$(1.03 \pm 0.44) \times 10^{-03}$
	-17.50 ± 0.500	$(7.10 \pm 1.95) \times 10^{-03}$
$z \sim 8$	-21.00 ± 0.500	$(5.34 \pm 5.34) \times 10^{-05}$
	-20.00 ± 0.500	$(2.70 \pm 2.06) \times 10^{-04}$
	-19.25 ± 0.250	$(3.15 \pm 2.27) \times 10^{-04}$
	-18.25 ± 0.250	$(1.97 \pm 0.78) \times 10^{-03}$
	-17.50 ± 0.500	$(2.84 \pm 1.09) \times 10^{-03}$
$z \sim 9$	-21.00 ± 0.500	$(1.97 \pm 8.90) \times 10^{-05}$
	-19.50 ± 0.500	$(5.49 \pm 3.45) \times 10^{-04}$
	-18.00 ± 0.500	$(1.33 \pm 0.99) \times 10^{-03}$
$z \sim 10$	-16.00 ± 0.500	$(5.35 \pm 2.72) \times 10^{-03}$

Note. Number densities were computed taking into account the redshift probability distribution for each candidate. Error bars included Poisson uncertainties and cosmic variance computed from Trenti & Stiavelli (2008) and the effective surface of our survey.

Table 8
Schechter Parameterization at $z \sim 7$, 8, 9, and 10

Redshift	$M^\star$ [AB]	α	$\Phi^\star$ [/mag/Mpc^{-3}]
$z \sim 7$	$-20.49^{+0.15}_{-0.11}$	$-2.00^{+0.13}_{-0.12}$	$(0.41^{+0.13}_{-0.14}) \times 10^{-3}$
$z \sim 8$	$-20.11^{+0.59}_{-0.25}$	$-1.76^{+0.35}_{-0.54}$	$(0.56 \pm 0.39) \times 10^{-3}$
$z \sim 9$	$-19.66^{+0.77}_{-0.44}$	$-1.48^{+0.32}_{-0.50}$	$(1.00^{+0.93}_{-0.77}) \times 10^{-3}$
$z \sim 10$	-20.28 (fixed)	$-2.23^{+0.24}_{-0.05}$	$(4.50^{+1.70}_{-1.9}) \times 10^{-5}$

Note. Schechter parameters deduced from this study using a χ^2 minimization method. Error bars are given by the 1σ confidence interval at $z \sim 7$, 8, 9, and 10.

($\pm$0.4) dex. Robertson et al. (2014) have shown that cosmic variance—because of the smaller source plane area being effectively probed with lensing—is higher and becomes quite significant in lensed fields. In that sense, LFs compiled from a single lensed field may be substantially biased compared to the blank field LFs. Fialkov & Loeb (2015) show that particularly for Lyman-break high-redshift galaxies, incompleteness from various factors including the surface-brightness slope of the lensed galaxies, is important to account for (for other discussions of such effects, see Wong et al. 2012; Atek et al. 2014; Ishigaki et al. 2015).

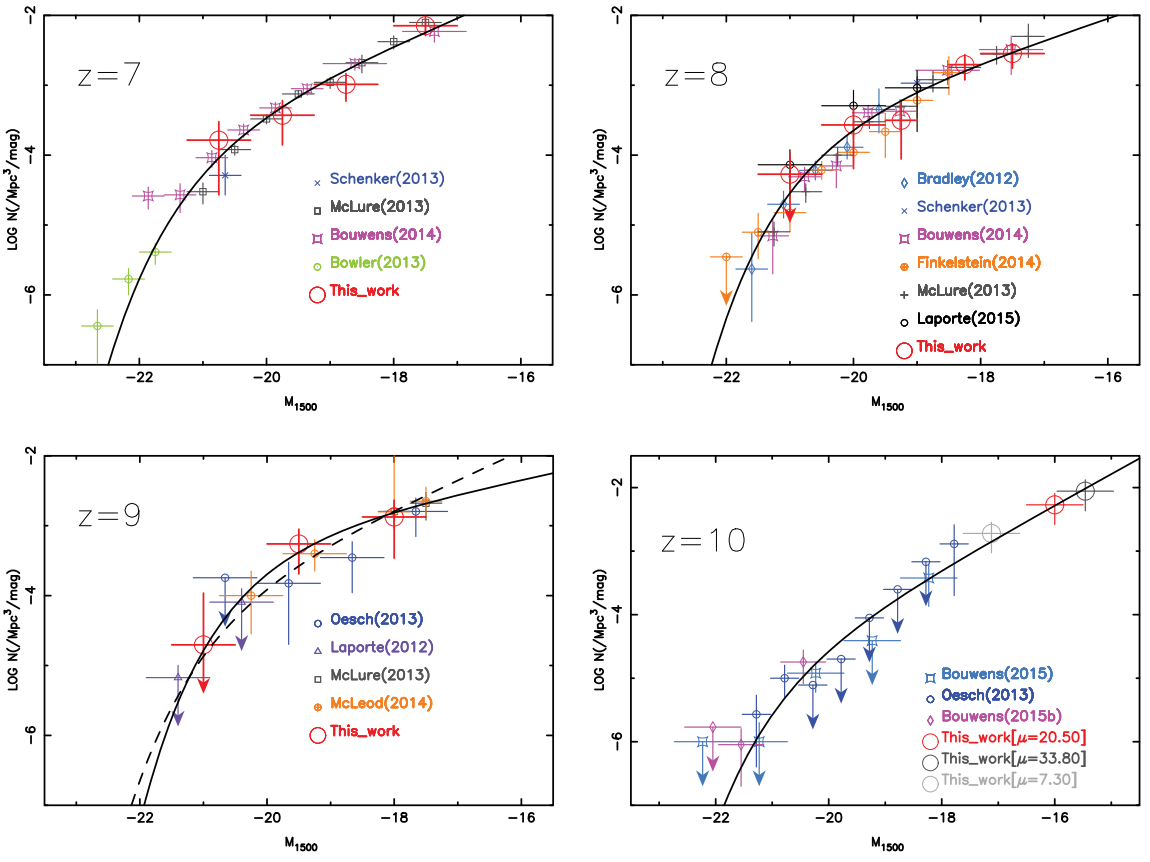

Figure 10. Shapes of the luminosity functions computed at $z \sim 7$, 8, 9, and 10 using samples selected from the M0416 cluster and parallel fields of the HFFs. In each case, the black line displays the best fit found using the densities computed in this study and other densities at the brightest luminosities published by other groups (see below). Upper left: LF at $z \sim 7$ including results from Schenker et al. (2013), McLure et al. (2013), Bouwens et al. (2015), and Bowler et al. (2014). The dashed line shows the parameterization computed by Bouwens et al. (2015). Upper right: LF at $z \sim 8$ including results from Schenker et al. (2013), Oesch et al. (2012), Laporte et al. (2015), Bouwens et al. (2015), Bradley et al. (2014), and Atek et al. (2014). The dashed line shows the parameterization computed by Bouwens et al. (2015). Lower left: LF at $z \sim 9$ including results from Bouwens et al. (2008), Oesch et al. (2012), Laporte et al. (2012), Zheng et al. (2012b), and McLure et al. (2013). The dashed line shows the parameterization computed by McLeod et al. (2014). Lower right: LF at $z \sim 10$ including results from Oesch et al. (2014) and Bouwens et al. (2015). The dashed line shows the parameterization assuming the α parameter found by Bouwens et al. (2015).

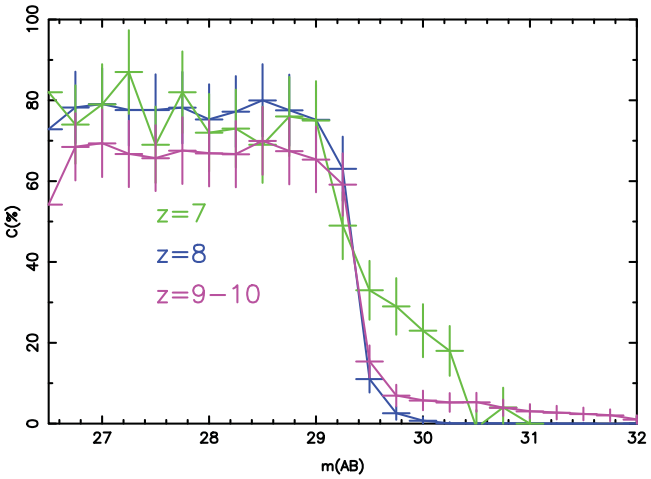

Figure 11. Completeness levels of our samples as a function of magnitude in the filter tracing the L_{1500} luminosity based on a mock catalog containing 680,000 objects with magnitudes ranging from 22 to 31 with redshifts ranging from 6.5 to 10.5 and assuming a log-normal distribution for the size of each object (see the text for details). Errors bars are deduced from the standard Poison uncertainties.

We adopted the Schechter parameterization (Schechter 1976) to study the evolution of the shape of the UV LF from $z \sim 7$ to 10. The three parameters were deduced using a χ^2 minimization approach using the densities estimated in this study combined with previous results. Errors bars at $z \sim 7$, 8, and 9 were deduced from the 1σ confidence interval. Given the paucity of objects currently known above $z \sim 10$, we fixed the value of $M^\star$ for the $z \sim 10$ LF to that adopted by Bouwens et al. (2015). Our parameterization is consistent with what is expected from the UV LF evolution (Bouwens et al. 2015). The shapes of the different LFs are shown in Figure 10 and the values of the three Schechter parameters are given in Table 8.

At $z = 10$, our candidate is located in a highly magnified region leading to a large 1σ error bar on the amplification. We took into account these uncertainties by computing the corresponding number densities over the amplification range covered by the 1σ interval. Figure 10 shows that the three constraints we deduce follow the same shape. However, to not bias the estimation of the Schechter parameters, we only fitted the UV LF using the density computed assuming the mean amplification ($\mu \sim 20.50$). We note that the best fit follows the shape described by both densities computed assuming different amplification values.

5.5. Comparison with Previous Studies

The HFF data for MACS0416 have been available since 2014 September, and two papers focusing on the brightest objects at $z \sim 8$ and 9 have been published recently (McLeod et al. 2014; Laporte et al. 2015). A key difference between our selection and the one used in Laporte et al. (2015) is the redshift interval covered by the color criteria. The selection window we used to select the highest redshift objects is well-defined over a redshift range between 6.5 and 10.5 (c.f. Figure 11) whereas Figure 2 of Laporte et al. (2015) shows that their window is primarily devoted to the selection of objects between 7.5 and 8.5. We note that two objects in our sample were not selected in Laporte et al. (2015). One of these, 1859, fails to satisfy the magnitude cut they applied, which only selects relatively bright candidates in the field. McLeod et al. (2014) selected five objects using a purely photometric redshift approach, among which four are in common with the sample described in this paper (491, 8428, 1213, and 1859 in our sample), while one object is not (ID = HFF2C-9-5). Note that our candidate 4008 is not in the redshift range they targeted.

6. CONCLUSIONS

In order to study the properties of young galaxies in the era of reionization, we characterize 22 galaxies between $z \sim 7$–10 discovered in the HFF M0416 cluster ($z = 0.396$) and parallel fields. Four of these galaxies were previously reported by Laporte et al. (2015) and four by McLeod et al. (2014). Our selection employed data from the *HST* optical, *J* and *H* bands, as well as deep HAWK-I/VLT K_s and IRAC 3.6 and 4.5 μm images. To find candidates, we carried out careful and strict color selection. Simulations indicate that the completeness in our sample ranges between 65% and 85% at redshifts between 7 and 10.0.

Photometric redshifts were calculated using a new version of the BPZ2.0. We develop a new quality criteria based on the ratio between peak early- and late-type galaxy probabilities ($\mathcal{R}$), and chose candidates with peak-probability ratios $\mathcal{R} \geqslant 3$. Furthermore, to test the reliability of our redshift estimations we used `iSEDfit`, which produced very similar results, with a mean difference of only $\Delta z = 0.1 \pm 0.1$ (`iSEDfit` minus BPZ2.0).

Magnifications are computed for the different candidates at the corresponding redshifts from a combination of six well selected models available in the MAST archive (see footnote 20). We looked for counter images for objects near critical curves. In the case of 8958, we search for images at two positions predicted by our models. Although there are some extremely faint red objects at these positions, no conclusive identifications could be reached.

Based on an SED analysis with `iSEDfit`, we computed stellar masses, SFRs, and ages for each candidate. Our $z > 7$ candidates are consistent with having mean stellar masses of $\log(M_*) \sim 8.44^{+0.55}_{-0.31}\,M_\odot$, SFRs of approximately $1.8^{+0.5}_{-0.4}\,M_\odot\,\mathrm{yr}^{-1}$, and SFR-weighted ages of $\lesssim 300^{+70}_{-140}$ Myr. These measurements agree with the results of Schaerer & de Barros (2010).

Finally, based on candidates in M0416 cluster and parallel fields, we computed LFs at $z = 7$, 8, 9, and 10. Thanks to the depth of HFFs, we are able to give the first direct estimates on the faint end of the UV LF at $z \sim 10$. The constraints given in Table 8 are clearly stronger than those in previous studies. This confirms the crucial role of the HFFs in detecting objects beyond the limits of current telescopes. The Schechter parameters are relatively well constrained at $z \sim 7$ and 8 regarding the number of objects in each samples. At higher redshifts, however, the full Frontier Fields data set will be required to increase the number of sources and reduce the cosmic variance effects.

The work presented in this paper is based on observations made with the NASA/ESA *Hubble Space Telescope*, and has been supported by award AR-13279 from the Space Telescope Science Institute (STScI), which is operated by the Association of Universities for Research in Astronomy, Inc. under NASA contract NAS 5-26555. It is also based on data obtained with the *Spitzer Space Telescope*, which is operated by the Jet Propulsion Laboratory, California Institute of Technology

under a contract with NASA. We acknowledge support from Basal-CATA PFB-06/2007 (L.I., F.E.B., N.L., S.K., and P.T.), FP7-SPACE-2012-ASTRODEEP-312725 (X.S.), NSFC grants 11103017 and 11233002 (X.S.), NASA through *Hubble* Fellowship grant *HST*-HF2-51334.01-A awarded by STScI (A.Z.), CONICYT-Chile grants FONDECYT 1141218 (F.E. B.), Gemini-CONICYT 32120003 (F.E.B. and N.L.), and "EMBIGGEN" Anillo ACT1101 (F.E.B.), the Ministry of Economy, Development, and Tourism's Millennium Science Initiative through grant IC120009, awarded to The Millennium Institute of Astrophysics, MAS (F.E.B.), Spanish consolider project CAD2010-00064 and AYA2012-39475-C02-01 (J.M. D.), the Brazilian funding agency-FAPESP post doc fellowship —process number 2014/11806-9 (A.M.) and CONICYT-Chile grant FONDECYT 3140542 (P.T.). L.I. would like to thank the European Southern Observatory and the University of Victoria, Canada, for providing office space while this work was done.

REFERENCES

Abrahamse, A., Knox, L., Schmidt, S., et al. 2011, ApJ, 734, 36
Atek, H., Richard, J., Kneib, J.-P., et al. 2014, ApJ, 786, 60
Benítez, N. 2000, ApJ, 536, 571
Bordoloi, R., Lilly, S. J., & Amara, A. 2010, MNRAS, 406, 881
Bouwens, R. J., Bradley, L. D., Zitrin, A., et al. 2014a, ApJ, 795, 126
Bouwens, R. J., Illingworth, G. D., Franx, M., et al. 2008, ApJ, 686, 230
Bouwens, R. J., Illingworth, G. D., Labbe, I., et al. 2011a, Natur, 469, 504
Bouwens, R. J., Illingworth, G. D., Oesch, P., et al. 2011b, ApJ, 737, 90
Bouwens, R. J., Illingworth, G. D., Oesch, P. A., et al. 2010, ApJL, 708, L69
Bouwens, R. J., Illingworth, G. D., Oesch, P. A., et al. 2012, ApJ, 737, 90
Bouwens, R. J., Illingworth, G. D., Oesch, P. A., et al. 2015, ApJ, 803, 34
Bouwens, R. J., Oesch, P. A., Labbe, I., et al. 2015, arXiv:1506.01035
Bowler, R. A. A., Dunlop, J. S., & McLure, R. J. 2014, MNRAS, 440, 2810
Bradley, L. D., Trenti, M., Oesch, P. A., et al. 2012, ApJ, 760, 108
Bradley, L. D., Zitrin, A., Coe, D., et al. 2014, ApJ, 792, 76
Broadhurst, T. J., Taylor, A. N., Peacock, J. A., et al. 1995, ApJ, 438, 49
Bruzual, G., & Charlot, S. 2003, MNRAS, 344, 1000
Burgasser, A. J., Cruz, K. L., Cushing, M., et al. 2010, ApJ, 710, 1142
Burgasser, A. J., McElwain, M. W., Kirkpatrick, J. D., et al. 2004, AJ, 127, 2856
Carrasco Kind, M., & Brunner, R. J. 2013, MNRAS, 432, 1483
Carrasco Kind, M., & Brunner, R. J. 2014, MNRAS, 442, 3380
Chabrier, G. 2003, PASP, 115, 763
Charlot, S., & Fall, S. M. 2000, ApJ, 539, 718
Coe, D., Benítez, N., & Sánchez, S. F. 2006, ApJS, 132, 926
Coe, D., Bradley, L., & Zitrin, A. 2015, ApJ, 800, 84
Coe, D., Zitrin, A., Carrasco, M., et al. 2013, ApJ, 762, 32
Coleman, G. D., Wu, C.-C., & Weedman, D. W. 1980, ApJS, 43, 393
Conroy, C., & Gunn, J. E. 2010, ApJ, 712, 833
Conroy, C., Gunn, J. E., & White, M. 2009, ApJ, 699, 486
Cunha, C. E., Lima, M., Oyaizu, H., Frieman, J., & Lin, H. 2009, MNRAS, 396, 2379
Diego, J. M., Broadhurst, T., Molnar, et al. 2015, MNRAS, 447, 3130
Ebeling, H., Edge, A. C., & Henry, J. P. 2001, ApJ, 553, 668
Ellis, R. S., McLure, R. J., Dunlop, J. S., et al. 2013, ApJL, 763, L7
Fan, X., Strauss, M. A., & Becker, R. H. 2006, AJ, 132, 117
Fazio, G. G., Hora, J. L., Allen, L. E., et al. 2004, ApJS, 154, 10
Fialkov, A., & Loeb, A. 2015, ApJ, 806, 256
Fioc, M., & Rocca-Volmerange, B. 1997, A&A, 326, 950
Hayes, M., Laporte, N., Pelló, R., et al. 2012, MNRAS, 425, 19
Illingworth, G. D., Magee, D., Oesch, P. A., et al. 2013, ApJS, 209, 6
Ishigaki, M., Kawamata, R., Ouchi, M., et al. 2015, ApJ, 799, 12
Jauzac, M., Clément, B., Limousin, M., et al. 2014, MNRAS, 443, 1549
Johnson, T. L., Sharon, K., Bayliss, M. B., et al. 2014, ApJ, 797, 48
Jouvel, S., Høst, O., Lehav, O., et al. 2014, A&A, 562, A86
Kawamata, R., Ishigaki, M., Shimasaku1, K., et al. 2015, ApJ, 804, 103
Kimble, R. A., MacKenty, J. W., O'Connell, R. W., & Townsend, J. A. 2008, Proc. SPIE, 7010, 70101E
Kinney, A. L., Calzetti, D., Bohlin, R. C., et al. 1996, ApJ, 467, 38
Koekemoer, A. M., Ellis, R. S., McLure, R. J., et al. 2013, ApJS, 209, 3
Laporte, N., Pelló, R., & Hayes, M. 2012, A&A, 542, L31
Laporte, N., Streblyanska, A., Kim, S., et al. 2015, A&A, 575, 92
Leitherer, C., Ekström, S., Meynet, G., et al. 2014, ApJS, 212, 14
Leitherer, C., Ortiz, P. A., Bresolin, F., et al. 2010, ApJS, 189, 309
Leitherer, C., Schaerer, D., Goldader, J. D., et al. 1999, ApJS, 123, 3
Lejeune, T., Cuisinier, F., & Busar, R. 1997, A&AS, 125, 229
Lejeune, T., Cuisinier, F., & Busar, R. 1998, A&AS, 130, 65
López-Sanjuan, C., Cenarro, A. J., Varela, J., et al. 2015, A&A, 576, 53
Lotz, J., Mountain, M., Grogin, N. A., et al. 2014, BAAS, 223, #25401
MacCracken, H., et al. 2012, A&A, 544A, 156
Madau, P. 1995, in Proc., ESO, QSO Absorption Lines, ed. G. Meylan (Berlin: Springer-Verlag), 377
Makovoz, D., & Khan, I. 2005, in ASP Conf. Ser. 132, Astronomical Data Analysis Software and Systems VI, ed. P. L. Shopbell, M. C. Britton & R. Ebert (San Francisco, CA: ASP), 81
McLeod, D. J., McLure, R. J., Dunlop, J. S., et al. 2014, MNRAS, 450, 3032
McLure, R. J., Dunlop, J. S., Bowler, R. A. A., et al. 2013, MNRAS, 432, 2696
Mandelbaum, R., Seljak, U., Hirata, C. M., et al. 2008, MNRAS, 386, 781
Mann, A. W., & Ebeling, H. 2012, MNRAS, 420, 2120
Molino, A., Benítez, N., Moles, M., et al. 2014, MNRAS, 441, 2891
Moustakas, J., Coil, A., Aird, J., et al. 2013, ApJ, 767, 50
Oesch, P. A., Bouwens, R. J., Illingworth, G. D., et al. 2010, ApJL, 709, L16
Oesch, P. A., Bouwens, R. J., Illingworth, G. D., et al. 2012, ApJ, 759, 1350
Oesch, P. A., Bouwens, R. J., Illingworth, G. D., et al. 2013, ApJ, 773, 75
Oesch, P. A., Bouwens, R. J., Illingworth, G. D., et al. 2014, ApJ, 786, 108
Peng, C. Y., Ho, L. C., Impey, C. D., & Rix, H.-W. 2010, AJ, 139, 2097
Pirard, J.-F., Kissler-Patig, M., Moorwood, A., et al. 2004, Proc. SPIE, 5492, 1763
Planck Collaboration, Ade, P. A. R., & Aghanim, N. 2015, arXiv:1502.01589
Polletta, M., Tajer, M., Maraschi, L., et al. 2007, ApJ, 663, 81
Postman, M., Coe, D., Benítez, N., et al. 2012, ApJS, 199, 25
Richard, J., Jauzac, M., Limousin, M., et al. 2014, MNRAS, 444, 268
Robertson, B. E., Ellis, R. S., Dunlop, J. S., et al. 2014, ApJ, 796, 27
Santini, P., Fontana, A., Grazian, A., et al. 2009, yCat, 350, 40751
Sanchez-Blázquez, P., Peletier, R. F., Jiménez-Vicente, J., et al. 2006, MNRAS, 371, 703
Schaerer, D., & de Barros, S. 2010, A&A, 515, 73
Schechter, P. 1976, ApJ, 203, 297
Schenker, M. A., Robertson, B. E., Ellis, R. S., et al. 2013, ApJ, 768, 196
Schmidt, K. B., Treu, T., & Trenti, M. 2014, ApJ, 786, 57
Scoville, N., Abraham, R. G., Aussel, H., et al. 2007, ApJS, 172, 38
Sheldon, E. S., Cunha, C. E., Mandelbaum, R., et al. 2012, ApJS, 201, 32
Silva, L., Granato, G. L., Bressan, A., et al. 1998, ApJ, 509, 103
Spitler, L. R., Straatman, C. M. S., Labbé, I., et al. 2014, ApJL, 787, LL36
Steidel, C. C., Adelberger, K. L., Giavalisco, M., et al. 1999, ApJ, 519, 1
Trenti, M., & Stiavelli, M. 2008, ApJ, 676, 767
Vázquez, G. A., & Leitherer, C. 2005, ApJ, 621, 695
Westera, P., Lejeune, T., Buser, R., Cuisinier, F., & Bruzual, G. 2002, A&A, 381, 524
Whitaker, K. E., Labbé, I., van Dokkum, P. G., et al. 2011, ApJ, 735, 86
Wittman, D. 2009, ApJL, 700, L174
Wong, K. C., Ammons, S. M., Keeton, C. R., & Zabludoff, A. I. 2012, ApJ, 752, 104
Wuyts, S., Labbé, I., Schreiber, N., et al. 2008, ApJS, 682, 985
Zheng, W., Bradley, L. D., Saraff, A., et al. 2012a, in Seventh Conference on Astronomical Data Analysis, 17
Zheng, W., Postman, M., Zitrin, A., et al. 2012b, Natur, 489, 406
Zheng, W., Shu, X., Moustakas, J., et al. 2014, ApJ, 795, 93
Zitrin, A., Meneghetti, M., Umetsu, K., et al. 2013, ApJ, 762, 30
Zitrin, A., Zheng, W., Broadhurst, T., et al. 2014, ApJL, 793, L12